The Seasonal Variability in the Semidiurnal Internal Tide; A Comparison between Sea Surface Height and Energetics

Harpreet Kaur[1], Maarten C. Buijsman[1], Zhongxiang Zhao[2], and Jay F. Shriver[3]

[1]School of Ocean Science and Engineering, University of Southern Mississippi, Stennis Space Center, Mississippi, USA
[2]Applied Physics Laboratory and School of Oceanography, University of Washington, Seattle, Washington, USA
[3]Ocean Dynamics and Prediction Branch, Naval Research Laboratory, Stennis Space Center, Mississippi, USA

Correspondence: Harpreet Kaur (harpreet.kaur@usm.edu)

Abstract. We investigate the seasonal variability of the semidiurnal internal tide steric sea surface height (SSSH) and energetics using 8-km global Hybrid Coordinate Ocean Model (HYCOM) simulations with realistic forcing and satellite altimeter data. In numerous previous studies, SSSH has been used to explore the seasonal changes in internal tides. For the first time, we compare the seasonal variability of the semidiurnal internal tide SSSH with the seasonal variability of the semidiurnal baroclinic
5 energetics. We explore the seasonal trends in SSSH variance, barotropic to baroclinic conversion rate, kinetic energy, available potential energy, and pressure flux for the semidiurnal internal tides. We find that the seasonal cycle of monthly semidiurnal SSSH variance in the Northern Hemisphere is out of phase with the Southern Hemisphere. This north-south phase difference and its timing are in agreement with altimetry. The amplitudes of the seasonal variability in SSSH variance are about 10-15% of their annual-mean values when zonally averaged. The normalized amplitude of the seasonal variability is higher for the SSSH
10 variance than for the energetics. The largest seasonal variability is observed in Georges Bank and the Arabian Sea, where the seasonal trends of monthly SSSH variance and energetics are in phase. However, outside these hotspots, the seasonal variability in semidiurnal energetics is out of phase with semidiurnal SSSH variance and a clear phase difference between the Northern and Southern Hemispheres is lacking. While the seasonal variability in semidiurnal energy is driven by seasonal changes in barotropic to baroclinic conversion, semidiurnal SSSH variance is also modulated by seasonal changes in surface stratification.
15 Surface intensified stratification at the end of summer enhances the surface perturbation pressures, which enhance the SSSH amplitudes.

1 Introduction

The interaction between surface tides and bathymetry, in the presence of density stratification, leads to the generation of internal tides (Huthnance, 1981; Baines, 1982; Gerkema and Zimmerman, 2008; Buijsman et al., 2020). These internal waves propagate
20 away from their generation sites and eventually dissipate. It is important to study internal tides as their dissipation may cause water mass mixing (Waterhouse et al., 2014; Melet et al., 2016), affecting the global ocean circulation (Munk and Wunsch, 1998; St. Laurent and Garrett, 2002). The mixing caused by internal tides also affects sediment transport (Sinnett et al., 2018) and the dispersal of nutrients (Tuerena et al., 2019). Internal tides from the deep ocean propagate towards the coast, where they break, scatter, and cause local mixing on the shelf . The forcing of regional models with remote internal tides enhances

25 ~~the coastal internal tide energy (Siyanbola et al., 2023).~~ (Siyanbola et al., 2023, 2024). Model simulations and in-situ observations have shown that internal tides feature temporal variability over ~~various~~ different timescales (Rainville and Pinkel, 2006; Shriver et al., 2014; Zaron and Egbert, 2014; Ponte and Klein, 2015; Buijsman et al., 2017; Zaron, 2017; Nelson et al., 2019; Löb et al., 2020; Zhao and Qiu, 2023; Solano et al., 2023; Yadidya et al., 2024). Ultimately, this variability may contribute to the time variability in ocean mixing. In this study, we compare the seasonal variability in semidiurnal steric sea 30 surface height (SSSH) with internal tide energetics in global ocean model simulations.

The seasonal variability in internal tides has been observed and simulated in numerous studies. Ray and Zaron (2011) noticed significant seasonal variations in internal tide sea surface height (SSH) in the northern South China Sea region using the in-phase component of the M_2 harmonic constant. The in-phase component of the internal tides has a constant phase and amplitude depending on the duration of the time series (Colosi and Munk, 2006; Ansong et al., 2015; Buijsman et al., 2020). 35 Zaron (2019) showed global maps of annual modulates of M_2 baroclinic SSH using satellite altimeter data and observed that seasonal variations are observed in the Arabian Sea, the region between the Seychelles and Madagascar, the South China Sea, and the region offshore of the Amazon River plume. The annual modulations of the M_2 internal tides create a signal at MA_2 and MB_2 frequencies, where MA_2 is M_2 minus the annual frequency and MB_2 is M_2 plus the annual frequency (Huess and Andersen, 2001; Zaron, 2019). Zhao (2021) used 25 years of global satellite altimeter data and observed that seasonal phase 40 variations are more dominant than seasonal amplitude variations for phase-locked internal tide SSH. Zhao (2021) also noticed strong seasonal variations in areas where a seasonal cycle in stratification is observed. Zhao and Qiu (2023) analyzed the seasonal variability of M_2 internal tides in the Luzon Strait. They suggested that ocean stratification and the Kuroshio current may be responsible for the seasonal variability.

Numerical model studies investigating the seasonal variability of the internal tide mainly focus on regional areas (Gerkema 45 et al., 2004; Jan et al., 2008; Osborne et al., 2011; Zaron and Egbert, 2014; Yan et al., 2020). Gerkema et al. (2004) observed seasonal dependence in the generation and propagation of the simulated internal tides in the Bay of Biscay region. They found that the area-integrated barotropic to baroclinic conversion rate is 15% higher in summer compared to winter, which can be attributed to the seasonal thermocline. Zaron and Egbert (2014) showed around 10% of seasonality in the mode 1 phase speed of M_2 internal tides in a simulation centered on the Hawaiian Ridge.

50 Only a few studies have used global numerical models to identify seasonal variability of internal tides (Müller et al., 2012; Shriver et al., 2014). Müller et al. (2012) used the STORMTIDE Model to show differences in the phase-locked M_2 internal tide SSH amplitude for summer and winter months. They found a root mean square error of the amplitude differences between the summer and winter seasons exceeding five millimeters in the western Pacific, around Madagascar, and the Bay of Bengal. Shriver et al. (2014) utilized the global Hybrid Coordinate Ocean Model (HYCOM) to study the seasonal variability in phase-55 locked M_2 internal tide SSH by calculating the annual cycle in amplitude. They observed significant seasonal variability in the amplitude of the M_2 internal tide in the Arabian Sea and the tropics.

The variability in the internal tide at the generation site can be due to seasonal fluctuations in barotropic tidal forcing (Liu et al., 2015) and stratification (Gerkema et al., 2004; Zhao, 2021; Schindelegger et al., 2022). Wind, stratification, or ice cover changes can impact the variability of barotropic tides over time (Kang et al., 2002; Müller et al., 2012; St. Laurent et al., 2008;

60 Bij de Vaate et al., 2021). Additionally, changes in stratification can affect the perturbation pressure, which, in turn, influences the rate of barotropic to baroclinic energy conversion. As the internal tides propagate, they can be influenced by the refraction of beams due to the temporal and spatial variability in eddies and stratification ~~(Ponte and Klein, 2015; Duda et al., 2018)~~ (Ponte and Klein, 2015; Buijsman et al., 2017; Duda et al., 2018), and dissipation (de Lavergne et al., 2019; Mukherjee et al., 2023).

65 The understanding of the seasonal variability in internal tides in the global ocean has been limited by the short duration of time series available from numerical experiments and the low spatial and temporal resolution of field measurements. While the ~~sea surface height (SSH)~~ SSH of internal tides has been used in previous studies to explore seasonal changes, the seasonal variability of internal tide SSH and energetics has never been compared. This study aims to answer the following questions: (a) Which areas in the global ocean have high seasonal variability in semidiurnal internal tides? (b) How do the spatial and

70 temporal variabilities in internal tide SSH and energetics from a global HYCOM simulation compare? (c) What explains their differences? (d) What mechanisms cause the seasonal variability? To answer these questions, we analyze the seasonal variability in semidiurnal internal tides using two global HYCOM simulations with output durations of ~~5 years and 1~~ five years and one year. We will examine the seasonal trends in SSSH variance, barotropic to baroclinic conversion rate, kinetic energy (KE), available potential energy (APE), and pressure flux for semidiurnal internal tides.

75 The rest of the paper is organized as follows: Section 2 explains the model simulation and the applied methodology. In section 3, we compare the seasonal variability in the semidiurnal SSSH variance with ~~that~~ the variability in the internal tide energetics. To confirm the accuracy of our findings, we also compare the ~~seasonal variability in the HYCOM simulation with the satellite altimeter observation~~ model results with satellite altimeter observations. Section 4 discusses the causes of the disparity in seasonal trends between SSSH variance and internal tide energetics. Finally, section 5 summarizes the study's key findings.

80 ## 2 Model and Methodology

2.1 Model Simulations

This study uses two existing global non-data assimilative HYCOM simulations~~(,~~ expt 06.1 and expt 18.5~~)~~, and an altimetry dataset. The list of datasets extracted from these simulations is given in Table 1. ~~We use various data products of these simulations that already exist. For the validation of the HYCOM simulation (Buijsman et al., 2017; Buijsman et al., 2020), we~~

85 ~~use the altimetry dataset from Zhao (2021)~~While we have a five-year SSSH time series from expt 18.5, we do not have the necessary three-dimensional (3D) fields to calculate the internal tide energy terms. To address this, we have utilized data from a shorter duration simulation, expt 06.1, which provides the required 3D fields.

2.1.1 Expt 06.1

For expt 06.1, the data is available for one year, from October 2011 to September 2012. We use SSSH and internal tide

90 energy terms from this simulation. This non-data assimilative simulation is forced with realistic atmospheric and tidal forc-

Table 1. List of datasets used in this study.

Model Name	Model/ Observation	Grid resolution [degrees]	Time series duration [years]	Products used in this study
Expt 06.1a	HYCOM	1/12.5	1 (10/2011-09/2012)	Hourly modal pressure and ~~baroclinic~~ velocity amplitudes. Monthly-mean horizontal velocity eigenfunctions and buoyancy frequency values. Monthly-mean global barotropic to baroclinic conversion rate, KE, APE, and baroclinic flux (not decomposed into modes). These data are extracted with methods discussed in Buijsman et al. (2020) and Raja et al. (2022).
Expt 06.1b	HYCOM	Subsampled at 6/12.5	1 (10/2011-09/2012)	Hourly time series of SSSH.
Expt 18.5	HYCOM	Subsampled at 0.5	5 (01/2005-12/2009)	Hourly time series of SSSH
ZHAO21	Altimetry	0.2	25 (1992-2017)	Harmonic constants of M_2 for 4 seasons from Zhao (2021)

ing (M_2, S_2, N_2, K_1, O_1). This simulation uses realistic atmospheric forcing from the NAVY Global Environmental Model (NAVGEM) (Hogan et al., 2014). The horizontal resolution is 8 km with 41 vertical layers. In expt 06.1, an Augmented State Ensemble Kalman Filter (ASEnKF) technique (Ngodock et al., 2016) is applied to improve the accuracy of barotropic tides. A parameterized topographic wave drag (Jayne and St. Laurent, 2001) and a scalar self-attraction and loading correction (SAL; Hendershott, 1972; Ray, 1998) are used. ~~Buijsman et al. (2017) and Buijsman et al. (2020) have discussed~~ The spin up time of the background circulation and tides for this model simulation ~~in detail.~~ is 15 years and two months, respectively (Buijsman et al., 2017). For more details on this simulation, the reader is referred to Buijsman et al. (2017) and Buijsman et al. (2020).

We use hourly SSSH snapshots subsampled at $6/12.5°$ to analyze the seasonal variability in the semidiurnal internal tide SSSH. We refer to this time series as expt 06.1b (Table 1). The monthly-mean and depth-integrated semidiurnal barotropic to baroclinic conversion rate, KE, APE, and baroclinic flux fields ~~are also~~ (not decomposed into modes) are computed by reconstructing harmonic timeseries for the sum of the M_2, S_2, and N_2 constituents. The ~~SSSH amplitude ratios~~ global-mean SSSH amplitude ratio of M_2:S_2:N_2 ~~are~~ is 1.0:0.44:0.30. ~~Hence, our analysis for both SSSH and energetics focuses on the semidiurnal band, which is dominated by M_2 (Egbert and Ray, 2003). The~~ In addition, the modal pressure and baroclinic velocity amplitudes, and horizontal velocity eigenfunctions are used to calculate mode 1 baroclinic (BC) SSH and energy terms. We refer to these data as expt 06.1a (Table 1).

2.1.2 Expt 18.5

We also use ~~5-year-long~~ five-year-long datasets from a global HYCOM simulation with a horizontal resolution of 8 km and 32 vertical layers to analyze the seasonal variability. This simulation features realistic atmospheric and tidal forcing. It is forced with four semidiurnal constituents (M_2, S_2, N_2, and K_2) and four diurnal constituents (K_1, O_1, P_1, and Q_1). This simulation is run from 2003 to 2011 with the atmospheric forcing from the Navy Operational Global Atmospheric Prediction System (NOGAPS) (Rosmond et al., 2002). A parameterized topographic wave drag (Arbic et al., 2010) and a scalar self-attraction and loading correction (SAL; Hendershott, 1972; Ray, 1998) are used. The spin up time of the background circulation and tides for this model simulation is 13 years and 13 months, respectively (Metzger et al., 2010; Buijsman et al., 2016). For more details on this simulation, the reader is referred to Shriver et al. (2012), Buijsman et al. (2016), and Nelson et al. (2019)~~have discussed this model simulation in detail~~.

To analyze the seasonal cycle in the semidiurnal internal tide SSSH, we use SSSH snapshots that are saved once per hour from 1 January 2005 to 31 December 2009. These snapshots are subsampled at $0.5°$ grid resolution.

2.2 Methodology

2.2.1 Seasonal variability in steric sea surface height

We analyze the seasonal variability in the semidiurnal SSSH. Steric SSH is ~~computed inline during~~ calculated in real-time as part of the HYCOM simulation (Savage et al., 2017). Although it has been shown in ~~Kaur (2024) and Zaron and Ray (2023)~~ Zaron and Ray (2023) and Kaur (2024) that the semidiurnal internal tide amplitude of SSSH is larger than the true semidiurnal internal tide SSH amplitude by about 20%, Kaur (2024) shows that the spatio-temporal variability is the same for ~~both SSHmetrics~~ the semidiurnal SSSH and the true semidiurnal internal tide SSH. We use a harmonic analysis to extract the M_2, S_2, and N_2 constituents, from which we calculate the semidiurnal signal. To extract the semidiurnal signal, we prefer the harmonic analysis over the bandpass analysis because the latter method also captures some mesoscale variance, particularly at higher latitudes (results not shown) ~~,~~ and numerical noise (thermobaric instability; Buijsman et al., 2020).

We extract monthly M_2, S_2, and N_2 amplitudes using the five-year hourly time series of SSSH from expt 18.5. Using a least-squares fit analysis, we compute the harmonic constants of the M_2, S_2, N_2, K_1, and O_1 constituents for each month (730 hours). The duration of 730 hours is long enough to resolve these five constituents. However, there is a possibility of tidal aliasing due to K_2 and P_1. This is because K_2 and S_2, and K_1 and P_1 both are separated by 2 cycles per year. It is important to note that this tidal aliasing only affects the semiannual ~~seasonal~~ signal for S_2, and not the annual signal (results not shown). The SSSH time series of the M_2, S_2, and N_2 internal tide can be written as

$$\eta_{\underline{i,m}}(t)_{\underline{m}} = \sum_j a_j(m)\cos(\omega_j \underline{t_i} t) + b_j(m)\sin(\omega_j t_{\underline{i}}), \tag{1}$$

where $i = 1,...,I$, I is the number of hours in the month m, ~~t is time~~, m is the index for each month, a and b are harmonic constants for the month and j refers to the M_2, S_2, N_2 constituents, ~~t represents time,~~ and ω is the frequency. The semidiurnal

SSSH variance for each month is calculated as

$$\sigma_{D2}^2(m) = \frac{1}{I}\sum_{i=1}^{I}\frac{1}{T}\int(\eta_{i,m})^2 dt. \tag{2}$$

where T is the number of hours in each month.

To calculate the seasonal variability in the semidiurnal internal tides SSSH variance, the annual cycle is fitted to the ~~5-year~~ five-year time series of the monthly semidiurnal SSSH variance (σ_{D2}^2) with a least-squares method after removing the linear trend

$$\hat{\sigma}_{D2}^2(m) = A_a \cos(\omega_a t_m - \phi_a), \tag{3}$$

where ω_a is the annual frequency, A_a and ϕ_a are the amplitude and phase of the annual signal, respectively, $\hat{\sigma}_{D2}^2$ is the fitted time series, $t_m = 30.42m$ ~~, m is the index for each month , which~~ and each month has 30.42 days.

We calculate the coefficient of determination (R^2) for the annual fit of the time series of the monthly variance. It identifies how much of the variability in the semidiurnal SSSH variance is due to the seasonality. The coefficient of determination for the fit is given by

$$R^2 = 1 - \frac{\sum_{m=1}^{M}[\sigma_{D2}^{2\prime}(m) - \hat{\sigma}_{D2}^2(m)]^2}{\sum_{m=1}^{M}[\sigma_{D2}^{2\prime}(m)]^2}, \tag{4}$$

where $\sigma_{D2}^{2\prime}(m)$ is the detrended time series of the monthly semidiurnal variance, and M is the total number of months.

2.2.2 Internal tide energetics

We analyze the seasonal variability in the semidiurnal internal tide energetics and compare it with the SSSH variance. Following ~~Buijsman et al. (2020)~~ Buijsman et al. (2017), we compute the monthly-mean and depth-integrated semidiurnal barotropic to baroclinic energy conversion rate, KE, APE, and baroclinic energy flux from hourly 3D data of expt 06.1a. ~~The semidiurnal band includes the~~ Initially, two sets of energy terms are computed for each month. For the first set, we bandpass the monthly time series of the 3D fields between 9 and 15 hours, compute the energy terms every hour, remove the first and last 24 hours to mitigate the effects of ringing, and finally average over time to compute the time-mean energy terms. For the second set, we bandpass the time series of the 3D fields between 9 and 15 hours, we extract the harmonic constants for the M_2, S_2, and N_2 constituents~~.~~, reconstruct the harmonic time series, compute the energy terms every hour, remove the first and last 24 hours to mitigate the effects of ringing, and finally average over time to compute the time-mean energy terms. The order of most steps is similar for both sets, which allows us to compare the total (bandpassed) internal tide energetics of the first set with the phase locked internal tide energetics of the second set (Buijsman et al., 2017). However, at high latitudes mesoscale motions and numerical noise adulterate the energetics of the first set. Hence, we use the second set based on the harmonic time series in this paper.

The depth-integrated and time-averaged internal tide energy balance equation is written as (Buijsman et al., 2016; Kang and Fringer, 2012)

$$\langle C \rangle = \langle \frac{\partial E}{\partial t} \rangle + \langle \nabla_h \cdot \mathbf{F} \rangle + \mathcal{R}, \tag{5}$$

where $\langle \rangle$ indicates the time-average over a month, C is the depth-integrated barotropic to baroclinic conversion, E is the depth-integrated total baroclinic wave energy, $\nabla_h \cdot \mathbf{F}$ is the horizontal divergence of the depth-integrated baroclinic energy flux $\mathbf{F} = (F_x, F_y)$, $\mathcal{R}$ is the residual, which is mostly due to baroclinic energy dissipation, and $\frac{\partial E}{\partial t}$ is the tendency term, which is ≈ 0 after time averaging. For periodic internal waves in the open ocean, the energy tendency is about zero when averaged over multiple tidal cycles (Buijsman et al., 2016; Buijsman et al., 2020).

The depth-integrated and time-averaged conversion of baroclinic tides from barotropic tides for each x, y coordinate is

$$\langle C \rangle = \frac{1}{T} \int_0^T W(z=-H,t) p'(z=-H,t) dt, \tag{6}$$

where $W(z=-H,t)$ is the vertical barotropic velocity at the sea floor, $p'(z=-H,t)$ is the perturbation pressure at the sea floor, z is the vertical coordinate, T is the number of hours in the month, and H is the water depth. The perturbation pressure is calculated as in Nash et al. (2005) and by removing the depth-mean pressure. The vertical barotropic velocity at the sea floor for each x, y coordinate is given by

$$W(z=-H,t) = -\mathbf{U}(t) \cdot \nabla_h H, \tag{7}$$

where $\mathbf{U} = (U,V)$ are the barotropic velocities in the x and y directions. The depth-integrated and time-averaged baroclinic flux for each x, y coordinate is calculated as

$$\langle \mathbf{F} \rangle = \frac{1}{T} \int_0^T \int_{-H}^0 \mathbf{u}'(z,t) p'(z,t) dz dt, \tag{8}$$

where $\mathbf{u}' = (u', v')$ are the horizontal baroclinic velocities in the x and y directions. The depth-integrated and time-averaged KE for each x, y coordinate is calculated as

$$\langle KE \rangle = \frac{1}{T} \int_0^T \int_{-H}^0 \frac{1}{2} \rho_0 (u'(z,t)^2 + v'(z,t)^2) dz dt, \tag{9}$$

where ρ_0 is the reference density. The depth-integrated and time-averaged APE for each x, y coordinate is calculated as

$$\langle APE \rangle = \frac{1}{T} \int_0^T \int_{-H}^0 \frac{g^2 \rho'(z,t)^2}{2\rho_0 N^2(z,t)} dz dt, \tag{10}$$

where g is the gravitational acceleration, N is the buoyancy frequency and ρ' is the perturbation density. The depth-integrated total baroclinic energy is the sum of depth-integrated KE and APE. The buoyancy frequency is calculated as

$$N^2 = -\frac{g}{\rho_0} \frac{\partial \langle \rho \rangle}{\partial z}, \tag{11}$$

where $\langle \rho \rangle$ is the mean potential density and $(\frac{\partial \langle \rho \rangle}{\partial z})$ is the vertical density gradient. In the remainder of the paper, we will drop the $\langle \rangle$ when discussing the time-averaged energy terms.

For expt 06.1, all variables (SSSH variance, barotropic to baroclinic conversion, KE, APE, total energy, and flux) are calculated for each month from October 2011 to September 2012. The exact number of hours per month is used. The hours for each month from October 2011 to September 2012 are as follows: 744, 720, 744, 744, 696, 744, 720, 744, 720, 744, 383, and 889. For August, we use the first two weeks of data because the model data for the third week ~~is missing~~was corrupted in storage. We add the ~~fourth week of data from~~ last week of August to September, resulting in ~~5~~ five weeks of data for September. However, the short months, February and August, show outlier values. The 14 days of August are not sufficient to resolve the M_2, S_2, and N_2 constituents, because M_2 has a beat period of 27.55 days with N_2. While February has 29 days, the mean is computed over 27 days because the tail ends of the time series are omitted. We believe that these two missing days may have impacted the energy values for the month of February globally. Therefore, we remove the monthly-mean values for February and August for each grid point and then linearly interpolate the values for these two months using data from adjacent months. The SSSH variance values are subsampled at 6/12.5° resolution. Hence, we also subsample KE, APE, total energy, and flux to 6/12.5° resolution.

2.2.3 Modal energetics

We decompose internal tide SSH and energetics into vertical modes to better understand the discrepancies in seasonal trends between SSSH variance and energy terms. For the calculation of mode 1 baroclinic SSH, KE, and APE, 3D HYCOM fields from expt 06.1a are decomposed into vertical modes following Buijsman et al. (2020) and Raja et al. (2022). The eigenfunctions of the first ~~5~~ five modes are computed for each month by solving the Stürm Liouville equation using the monthly-mean and spatially varying buoyancy frequency (Gerkema and Zimmerman, 2008). The horizontal velocity eigenfunctions are projected onto the perturbation pressure and baroclinic velocity time series to obtain a modal amplitude time series for pressure and velocities.

To compare with SSSH, we compute the mode 1 SSH. For each x, y coordinate applies

$$p_1(z, t) = \tilde{p}_1(t)\mathcal{U}_1(z), \tag{12}$$

where p_1 is the mode 1 pressure, $\tilde{p}_1(t)$ is the mode 1 amplitude time series of pressure, and $\mathcal{U}_1(z)$ is the horizontal velocity eigenfunction of mode 1. The mode 1 SSH is calculated as

$$\eta_1(t) = \frac{p_1(z=0, t)}{g\rho_0}. \tag{13}$$

We extract the harmonic constants for the M_2, S_2, and N_2 internal tide from the hourly time series of mode 1 SSH and bottom perturbation pressure ($p_1(z = -H, t)$) for each month. Then, the variance for semidiurnal mode 1 SSH and bottom perturbation pressure is calculated using Eqs. (1) and (2).

For calculation of the mode 1 semidiurnal KE and APE, we extract the harmonic constants for M_2, S_2, and N_2 constituents for each month from the time series of the mode 1 amplitudes of baroclinic velocities and pressure. The mode 1 semidiurnal

KE and APE are calculated as (Kelly et al., 2012)

$$KE_1 = \sum_j (|\hat{u}_{1j}|^2 + |\hat{v}_{1j}|^2)\frac{H\rho_0}{4}, \tag{14}$$

$$APE_1 = \sum_j (1 - \frac{f^2}{\omega_j^2})\frac{|\hat{p}_{1j}|^2}{c_1^2\rho_0}\frac{H}{4}, \tag{15}$$

where $\hat{u}_{1j}$, $\hat{v}_{1j}$, and $\hat{p}_{1j}$ are the mode 1 complex harmonic constants of the baroclinic velocities and perturbation pressure for
215   constituent j, c_1 is the mode 1 eigenspeed, and f is the Coriolis frequency.

The mode 1 variables are also linearly interpolated for February and August for each grid point using the same methodology
as we employed for the undecomposed fields. Additionally, we subsample these variables to 6/12.5° resolution to compare
with the SSSH variance.

2.2.4   Satellite altimeter data

220   We validate the seasonal variability in the HYCOM mode 1 M_2 baroclinic SSH variance and KE with the satellite altimeter data
of Zhao (2021). Zhao (2021) analyzed the seasonal variability of the mode 1 M_2 internal tide using 25 years of multisatellite
altimeter data from 1992 to 2017. Zhao (2021) could only extract mode 1 M_2 amplitudes with reasonable accuracy for 4
seasons: winter (January, February, and March), spring (April, May, and June), summer (July, August, and September), and
fall (October, November, and December). Thus, the satellite observations may underestimate the amplitudes of the seasonal
225   variability. The variance for each season is calculated as

$$\sigma_s^2 = \frac{A_s^2}{2}, \tag{16}$$

where A_s is the mode 1 M_2 internal tide SSH amplitude for season s.

3   Results

3.1   Spatial variability in SSSH and energy

The mean over 12 months for semidiurnal SSSH variance, depth-integrated semidiurnal barotropic to baroclinic conversion
230   rate, depth-integrated semidiurnal baroclinic energy, and depth-integrated semidiurnal baroclinic flux for expt 06.1 are shown
in Figure 1. The baroclinic energy and flux values are subsampled at 6/12.5° to compare with the SSSH variance.

The barotropic to baroclinic conversion rate in Figure 1b is higher at ridges and rough topography, highlighting the in-
ternal tide generation sites. SSSH variance, energy, and flux values are also higher near the generation sites (Figure 1).
The patterns for APE and KE (not shown) are the same as total energy (Figure 1c). The polygon in Figure 1c marks an
235   area in the North Pacific with elevated KE, which may be attributed to thermobaric instabilities (TBI). TBI is a numerical
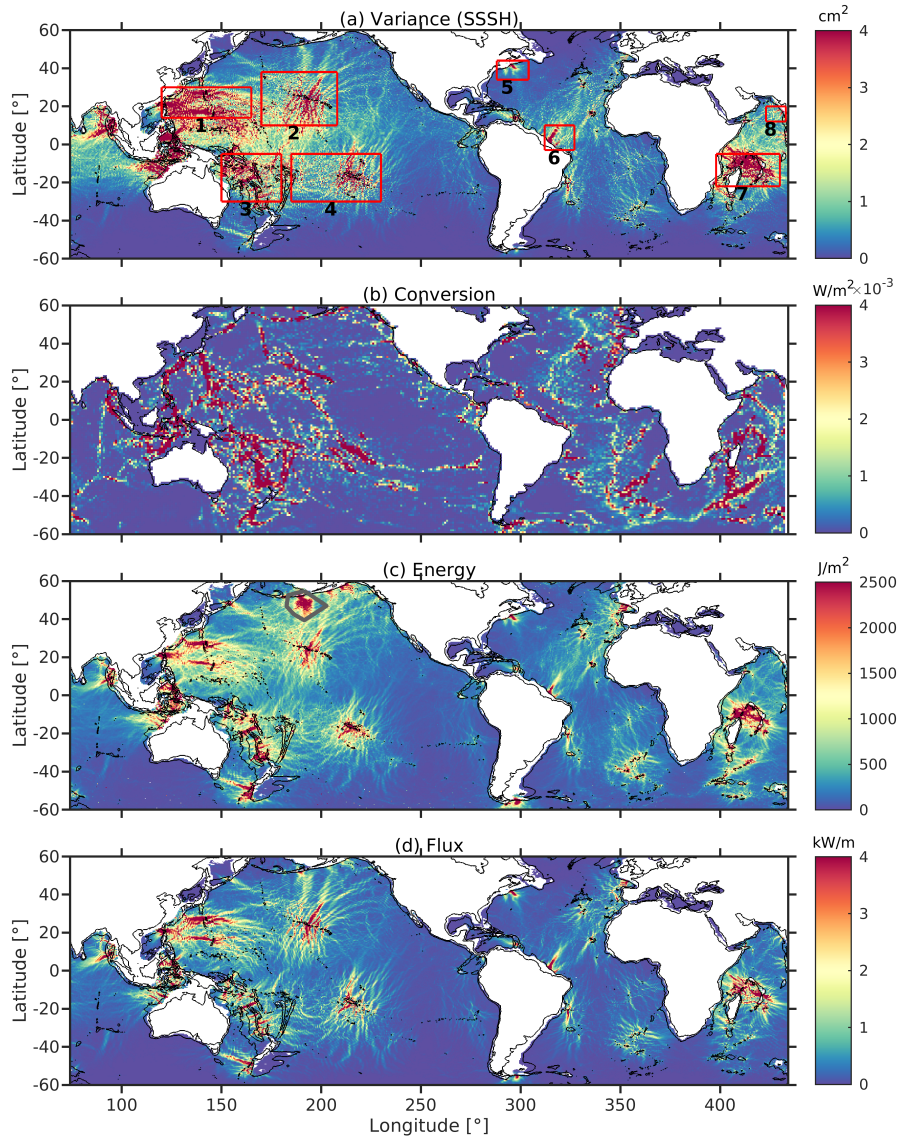
Figure 1. (a) Monthly semidiurnal SSSH variance, (b) depth-integrated semidiurnal barotropic to baroclinic conversion rate, (c) baroclinic semidiurnal energy, and (d) baroclinic semidiurnal flux of expt 06.1 averaged over 12 months. In (a), (c), and (d), black bathymetry contours are plotted at 0 m and 2000 m. In (a), the following regions are marked: (1) East of Philippines, (2) Hawaii, (3) Tropical SW Pacific, (4) Tropical South Pacific, (5) Georges Bank, (6) Amazon Plume, (7) Madagascar, and (8) Arabian Sea. In (b), conversion rates are area-averaged to 1° grid resolution, and black bathymetry contours are plotted at 0 m. In (c), the gray polygon marks the area affected by thermobaric instabilities.

instability present in Lagrangian/isopycnic vertical coordinate ocean models due to inaccurate compensation for compressibility in calculating pressure gradient accelerations (Hallberg, 2005). TBI is known to occur in the North Pacific Ocean ~~(Buijsman et al., 2016; Buijsman et al., 2020)~~ in both expt 06.1 and expt 18.5 (Buijsman et al., 2016; Buijsman et al., 2020). Although TBI is a broadband signal with a variable phase, it is possible that some of this noise projects on the harmonic constants. We omit the area with TBI because it adversely impacts the seasonal variability analysis.

3.2 Seasonal variability in steric sea surface height

The first objective is to analyze the seasonal variability in semidiurnal internal tide SSSH variance. We use the detrended monthly variance ($\sigma_{D2}^{2\prime}$) of the combined M_2, S_2, and N_2 internal tides, which is computed with hourly time series of SSSH from expt 18.5. We use expt 18.5 because this simulation has a ~~5-year~~ five-years duration, which benefits the calculation of the annual seasonal cycle. Using a least-squares fit analysis, we calculate the annual cycle in the monthly variance of semidiurnal internal tide SSSH. The amplitude of the annual cycle is normalized by the mean semidiurnal variance over 60 months (Figure 2a). We are using the normalized amplitude (Figure 2a) and R^2 (Figure 2c) as indicators for the seasonal variability. If the normalized amplitude is small, the variance does not vary much seasonally. Hence, we focus on areas where both the normalized amplitude and R^2 are significant.

The internal tides generated in the coastal areas of Georges Bank and the Arabian Sea display the largest seasonal variability (Figure 2a and c). Figure 2b shows that the seasonal cycle of the semidiurnal internal tide SSSH variance in the Northern Hemisphere is 180° out of phase with the variance in the Southern Hemisphere. ~~This indicates~~ If the phase is 90° (-90°), the semidiurnal SSSH variance is maximum in April (October), which implies internal tides are stronger in respective fall months in the Northern and Southern Hemispheres. This suggests that seasonal changes in the semidiurnal SSSH variance may be due to stratification, which can affect the propagation and/or generation of the internal tides. In the next section, we investigate whether the same seasonal variability is present in the internal tide energetics.

3.3 Seasonal variability in internal tide energetics

In this section, we analyze the seasonal trend in semidiurnal internal tide energetics and compare it with the seasonal trend in semidiurnal SSSH variance. To do so, we use one-year data from expt 06.1 to calculate the monthly semidiurnal SSSH variance, depth-integrated conversion rate, KE, APE, energy, and flux for M_2, S_2, and N_2 constituents. Unfortunately, the annual cycle fit similar to Figure 2 for the internal tide energetics is very noisy because one year of data is insufficient to fit the annual signal accurately. Hence, we do not show these results.

To better visualize the seasonal trends, we zonally average the conversion rate, flux, SSSH variance, KE, APE, and total energy over 10-degree latitude bins for the Atlantic and the Pacific Oceans for each one-month period. The values in areas shallower than 100 m are excluded from the analysis. This is because the model does not resolve internal tides satisfactorily in these areas. To derive the anomaly time series for these variables, we remove and normalize by their annual-mean values. The anomaly plots are presented in Figures 3 and 4 for the Pacific and Atlantic Oceans, respectively. In Appendix A, we calculate the zonally averaged SSSH variance anomaly time series from expt 18.5 for all five years, following a similar approach as for
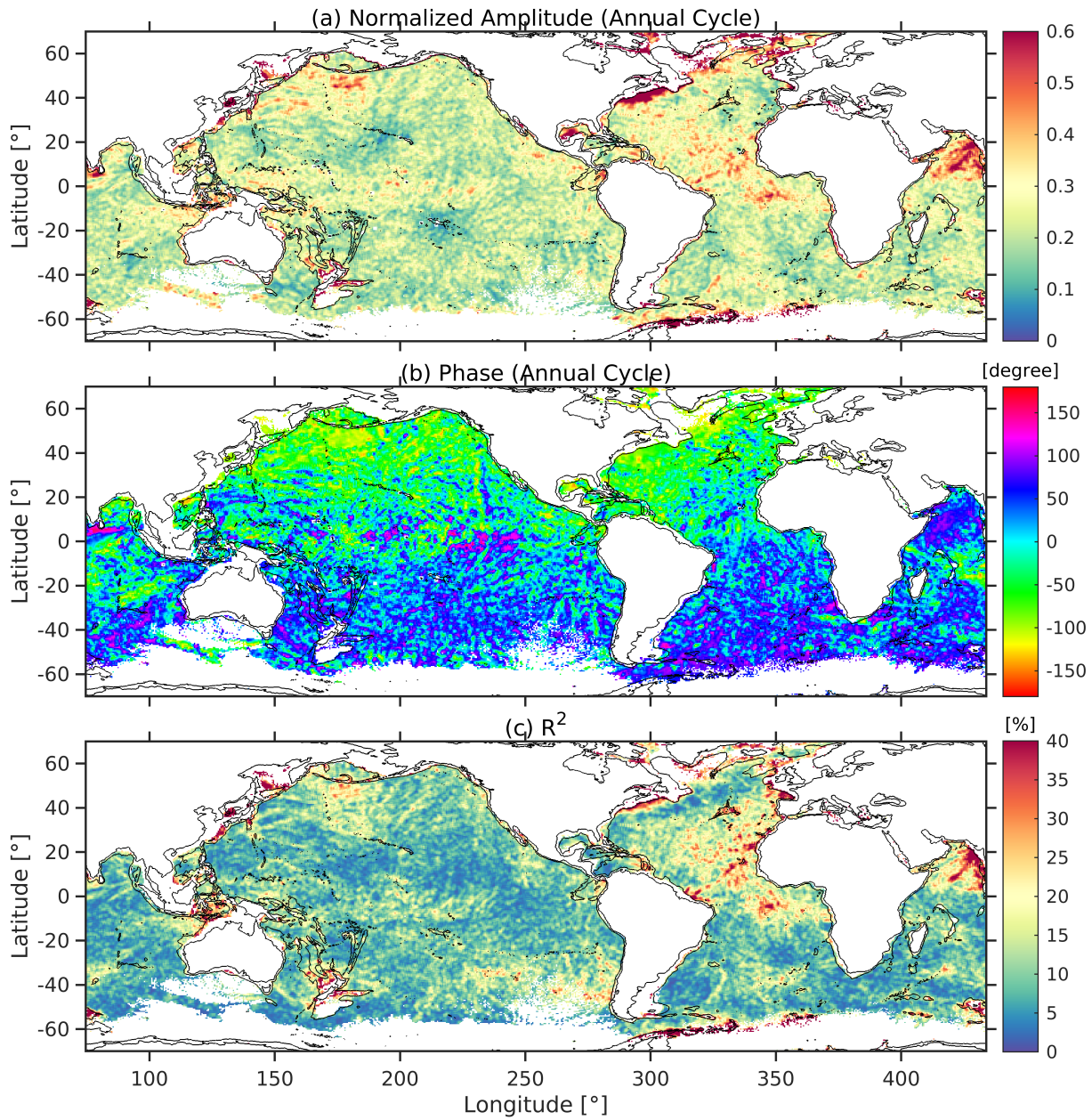
Figure 2. (a) The normalized amplitude and (b) phase of the annual cycle of the monthly semidiurnal SSSH variance ($\sigma^{2\prime}_{D2}$). (c) The coefficient of determination (R^2) for the fit. Black bathymetry contours are plotted at 0 and 2000 m. The normalized amplitude, phase, and R^2 ~~of the fit~~ are computed for each point and smoothed by taking a 9-point (3x3 square box) running mean. The areas with small internal tides (mean monthly variance < 0.01 cm^2) are removed. Data is from expt 18.5.
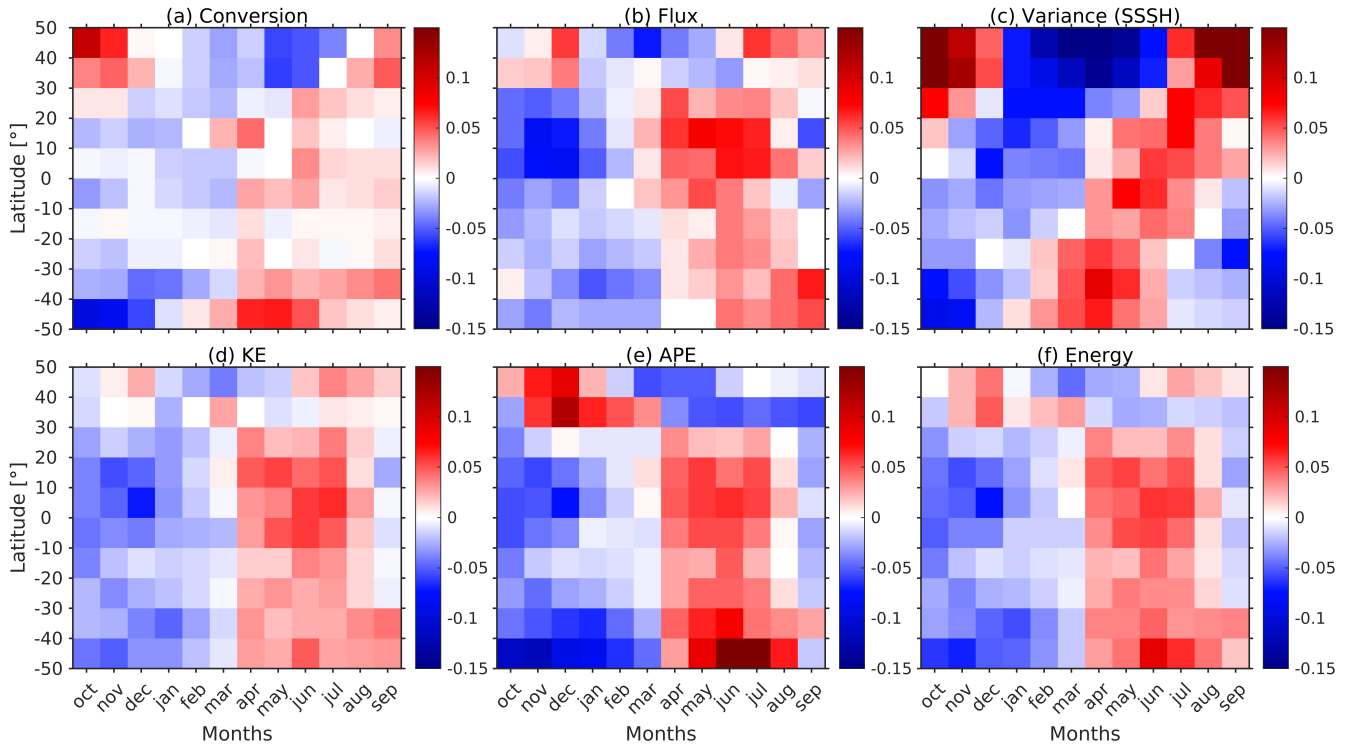
Figure 3. Zonally averaged anomaly time series of monthly semidiurnal (a) barotropic to baroclinic conversion rate, (b) baroclinic energy flux, (c) SSSH variance, (d) KE, (e) APE, and (f) total energy for the Pacific Ocean. The anomalies are computed by removing and normalizing by the annual-mean values. Data is from expt 06.1.

A seasonal cycle is observed in all variables (conversion rate, flux, SSSH variance, KE, APE, and total energy) in both the Pacific and Atlantic oceans (Figures 3 and 4). While the seasonal trends are broadly similar for the energy terms in both oceans, they differ from the trends in the SSSH variance. Similar to Figure 2b, the seasonal cycle of the SSSH variance is out of phase in the Northern and Southern Hemispheres in Figures 3 and 4. In contrast, the energy terms do not follow the same trends for the two hemispheres. The seasonal cycles of the energy terms are out of phase with SSSH variance, and no apparent
275   differences are present between the Northern and Southern Hemispheres. However, both SSSH and energetics tend to show the largest amplitudes at higher latitudes.

The amplitude of the seasonal cycles in Figures 3 and 4 is maximally about 15% of the annual-mean value. The percentage change is higher for the SSSH variance as compared to the conversion rate and KE. The percentage change for APE is also
280   larger than the conversion rate and KE at higher latitudes. For a free-propagating internal tide, $\frac{KE}{APE} = \frac{\omega^2 + f^2}{\omega^2 - f^2}$ (Alford and Zhao, 2007). As $\omega \approx f$ at higher latitudes, APE tends to 0. Therefore, APE is small at higher latitudes, and the percentage change
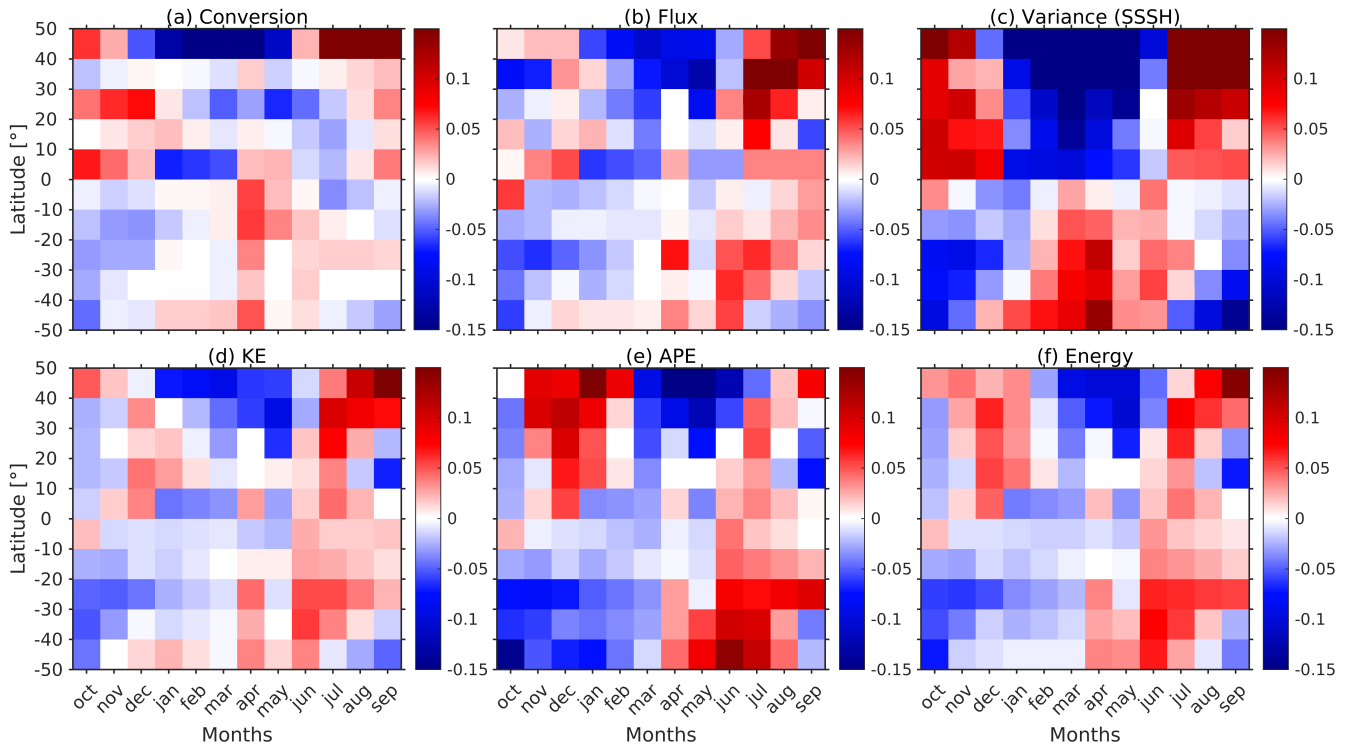
Figure 4. The same as Figure 3, but for the Atlantic Ocean.

for APE is large. To determine that the normalization is not misrepresenting the seasonal signal, we show the non-normalized anomalies in Figures B1 and B2 in Appendix B. These figures show that the seasonal trends remain consistent. However, there is a difference in the amplitude because if the internal tide signal is small (large), it can increase (decrease) the percentage

285 change. Additionally, it is important to emphasize that this study focuses primarily on trends and percentage change; therefore, utilizing the normalized data is preferable.

In the Pacific Ocean, the seasonal signal for the SSSH variance in the tropical region, spanning from -20° to 20°, is marginally out of phase when compared to the polar regions (Figure 3c). In this region, the seasonal signal in the SSSH variance is in sync with the internal tide energetics. In the Atlantic Ocean (Figure 4), the seasonal cycle for energy terms is noisier than in the

290 Pacific Ocean. This may be because the internal tide generation is weaker in the Atlantic Ocean, with most of the generation happening at deep ridges. The strong seasonal signal in the conversion between 40°N to 50°N in Figure 4a (and B2a) is attributed to Georges Bank.

To further compare the seasonal signals, we plot in Figure 5 the area-averaged semidiurnal SSSH variance, KE, and conversion anomalies for each month for eight regions (red boxes in Figure 1a). The seasonal signal of KE and conversion is similar

295 to that of the SSSH variance for Georges Bank and the Arabian Sea, where the strongest seasonal variability in internal tides is observed (Figure 5i, j, o, and p). The strong seasonal variability in conversion rate in the Arabian Sea and Georges Bank
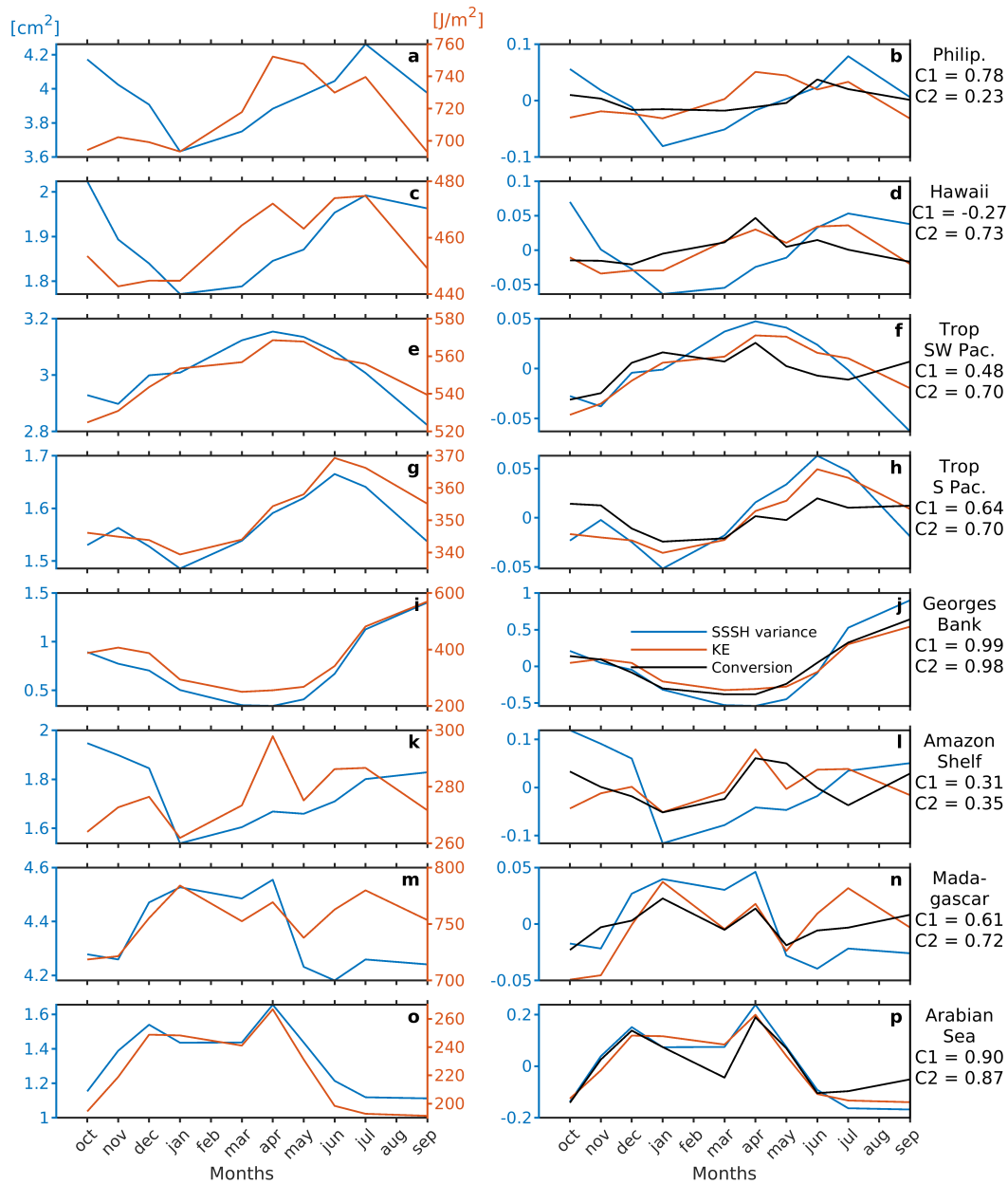
Figure 5. Area-averaged (left column) monthly semidiurnal SSSH variance (blue line) and KE (orange line) and (right column) normalized anomaly time series of monthly semidiurnal SSSH variance (blue line), KE (orange line), and conversion (black line) for regions marked by the red square boxes in Figure 1a. C1 and C2 are the correlation coefficients between SSSH variance and conversion, and between KE and conversion, respectively. Data is from expt 06.1.

and their relation to the stratification are further explained in Appendix C. The seasonal amplitudes of SSSH variance, KE, and conversion at Georges Bank and the Arabian Sea are ~50% and ~20%, respectively. This percentage is obtained from the normalized anomaly time series shown in the right column of Figure 5. The correlation coefficient between SSSH variance and conversion at Georges Bank and the Arabian Sea is 0.99 and 0.90, respectively. However, for the Tropical SW Pacific and the Tropical South Pacific (Figure 5e, f, g, and h), the seasonal signal of KE is similar to the SSSH variance but with a phase lag. For other regions, the discrepancies are more complex. Overall, the conversion shows a better correlation with KE than SSSH variance, except east of the Philippines, where the correlation coefficient between KE and SSSH variance (0.78) is higher than between KE and conversion (0.23).

Our analysis indicates that the conversion rate is the primary factor responsible for the seasonal variability in internal tide energetics because the seasonal trends of conversion and ~~KE~~ other energy terms are similar. The amount of internal tide energy in the ocean is governed by the internal tide energy input at topography, which is computed with the conversion metric. However, the seasonal trends of SSSH variance are different from ~~those of conversion and~~ the trends in the energy terms, except for Georges Bank and the Arabian Sea, where the seasonal variability is ~~strong. In the~~ the strongest. In Appendix C, we discuss the seasonal cycles in conversion in Georges Bank and the Arabian Sea, and the environmental drivers in more detail. In the next section, we will validate the seasonal variability in HYCOM with altimetry to ensure that the seasonal variability in HYCOM sea surface height is realistic. In the discussion section, we will explain the observed ~~difference~~ differences in the seasonal variability between SSSH variance and internal tide energetics ~~in other regions~~.

3.4 Comparison with the satellite altimeter data

To validate the seasonal variability in our model, we compare the ~~HYCOM output with the satellite altimeter data from Zhao (2021). Zhao (2021) analyzed the seasonal variability of the~~ mode 1 M_2 internal tide ~~using satellite altimeter data. We compare the mode 1 M_2 internal tide~~ variance from the satellite altimeter data from Zhao (2021) for each season with the mode 1 M_2 SSH variance and mode 1 M_2 KE from the HYCOM simulation expt 06.1a in Figure 6. It is discussed and shown later that semidiurnal ~~SSSH and~~ mode 1 SSH variance and semidiurnal SSSH variance are in good agreement. To ensure accuracy, we omit areas with strong mesoscale activity from the satellite altimeter and HYCOM data. Additionally, we interpolate the mode 1 M_2 SSH variance and KE from the HYCOM simulation to the same locations as the altimetry data for each season. We then zonally average the M_2 variance from the satellite altimeter data, the M_2 baroclinic SSH variance, and the KE over $10°$ latitude bins for the Atlantic and the Pacific Oceans for each season, while also removing regions of weak internal tides (~~As~~ as in Zhao (2021), areas with M_2 internal tide SSH amplitude < 0.2 cm are removed)~~for all variables~~. Finally, we remove and normalize by the annual-mean. ~~The results are presented in Figure 6.~~

The seasonal variability of both HYCOM and satellite altimeter M_2 SSH variance for the Pacific and Atlantic Oceans are in reasonable agreement. However, the level of agreement between the two is stronger in the Atlantic Ocean than in the Pacific Ocean. Moreover, the seasonal SSH variance of the satellite altimeter data is noisier than the HYCOM SSH variance. The reasons for this are not clear to us. It could be attributed to the sparseness of the satellite altimeter data in time and space. Despite these discrepancies, the trends observed in KE are different from both the HYCOM and satellite altimeter SSH
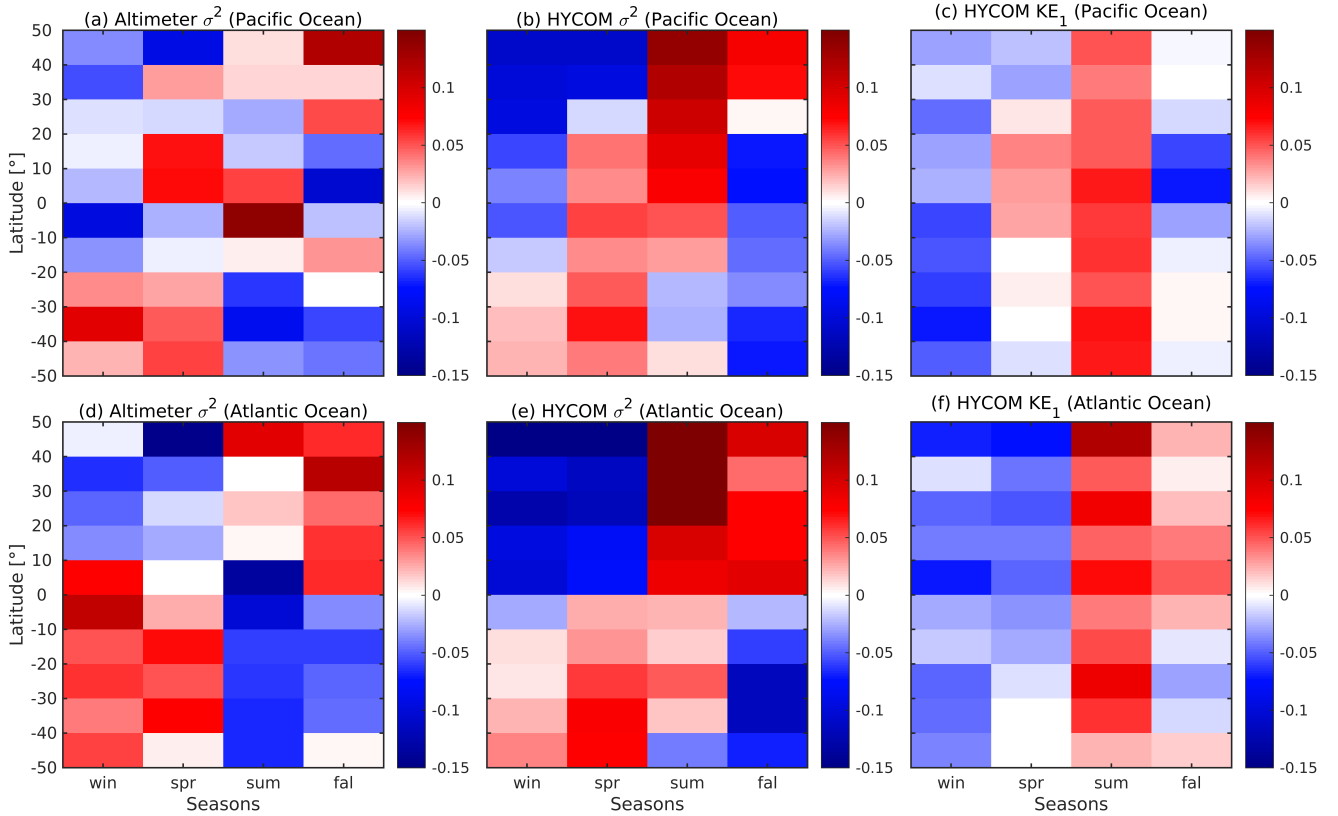
Figure 6. Zonally averaged normalized anomaly time series of seasonal-mean mode 1 M_2 internal tide SSH variance for (a and d) the satellite altimeter data and (b and e) the HYCOM expt 06.1 data, and (c and f) mode 1 M_2 KE from HYCOM expt 06.1. The anomaly time series for the Pacific Ocean are in (a-c) and for the Atlantic Ocean are in (d-f).

variance, indicating that the seasonal variability in KE is different from the internal tide SSH variability. This comparison suggests that the trends in baroclinic SSH variance in HYCOM are realistic but that they do not reflect the seasonal variability of the energy in the internal tide except in Georges Bank and the Arabian Sea (Figure 5).

4 Discussion

335   In this section, we explore the causes of the differences in the seasonal variability between SSSH variance and the energy terms. SSSH is strongly affected by the density of the surface layers, which varies significantly due to seasonal temperature changes (Qu and Melnichenko, 2023). Based on our analysis, the seasonal changes in semidiurnal SSSH variance may not accurately represent the actual seasonal changes in internal tide energy because the internal tide SSH may be modulated by changes in surface temperature. To understand this better, we compare the seasonal variability in SSSH variance to mode 1 SSH variance,

340   KE, APE, bottom perturbation pressure variance, and depth-mean buoyancy frequency.

We compute the mode 1 semidiurnal baroclinic SSH variance, bottom perturbation pressure variance, KE, and APE for each month using 3D fields from expt 06.1a. These variables are based on reconstructed time series for the M_2, S_2, and N_2 constituents. We consider mode 1 because the internal tide SSSH is dominated by mode 1 (Zhao et al., 2019; Buijsman et al., 2020). The spatial patterns of the time-mean bottom perturbation pressure variance are similar to the time mean semidiurnal SSSH variance in Figure 1a and is not shown.

We compare the seasonal trends in semidiurnal SSSH variance, mode 1 semidiurnal baroclinic SSH variance, KE, APE, bottom perturbation pressure variance, and N^2 for the Pacific and Atlantic Oceans in Figures 7 and 8. We zonally average these variables over 10-degree latitude bins for each basin and one-month segment. For all variables, shallow areas are removed (depth $<$ 100 m). To derive the anomaly time series, we remove and normalize by the annual-mean values. We consider the seasonal variability in the bottom perturbation pressure variance to better understand the effect of surface stratification on the SSSH variance. As expected, the undecomposed SSSH and mode 1 SSH variance have identical spatial and seasonal trends in Figures 7b, c and 8b, c. In contrast, for both the Atlantic and Pacific Oceans, the seasonal variability in bottom perturbation pressure variance resembles that of the energy terms and not that of the mode 1 SSH variance, which is based on the surface perturbation pressure. Interestingly, the seasonal trend in the depth-mean buoyancy frequency is similar to the SSSH variance and mode 1 SSH variance, but it is 1-2 months ahead of the SSSH variance. The seasonal signal in the buoyancy frequency is out of phase in the Northern and Southern Hemispheres, which is similar to what we observe for the SSSH variance.

The mode 1 SSH is computed as $\frac{\tilde{p_1}(t)\mathcal{U}_1(z=0)}{g\rho_0}$. To understand what is modulating the semidiurnal mode 1 SSH variance, we study the seasonal trend in mode 1 horizontal velocity eigenfunction at $z=0$ and the variance of the semidiurnal mode 1 perturbation pressure amplitude for the Pacific and Atlantic Oceans (Figure 9). The seasonal trends in $\mathcal{U}_1^2(z=0)$ are similar to the mode 1 SSH variance. The area-averaged correlation coefficient between the mode 1 SSH variance and $\mathcal{U}_1^2(z=0)$ is 0.84 and 0.89 for the Pacific and Atlantic Oceans, respectively. Moreover, the seasonal variability of $\mathcal{U}_1^2(z=0)$ is similar to the depth-averaged buoyancy frequency anomaly in Figures 7a and 8a. Specifically, when the buoyancy frequency is surface intensified at the end of summer, $\mathcal{U}_1^2$ is also surface intensified. Therefore, we conclude that the surface density stratification is the main factor that modulates the seasonal variability in semidiurnal SSSH variance. In contrast, the variance of the semidiurnal mode 1 perturbation pressure amplitude ($\tilde{p_1}$) in Figure 9c and f is more in agreement with the mode 1 KE and APE variability in Figures 7 and 8. We note that $\mathcal{U}_1(z)$ does not contribute to the depth-integrated monthly values of mode 1 KE and APE because of the normalization condition ($\frac{1}{H}\int_{-H}^{0}\mathcal{U}_1^2(z)dz=1$; Buijsman et al., 2020). Hence, the seasonal effect due to stratification observed for surface values of $\mathcal{U}_1$ disappears when depth-integrating.

Alternatively, we can also explain the modulation by considering APE. If we assume that the barotropic-to-baroclinic conversion rate remains constant throughout the year, we can assume that APE is constant. APE is proportional to $\frac{\rho'(z,t)^2}{N^2(z,t)}$ (Eq. 10). If there is an increase (decrease) in surface temperature, N also increases (decreases), which means that $\rho'(z,t)$ will also increase (decrease) for APE to remain constant. This increase (decrease) in $\rho'(z,t)$ results in an increase (decrease) in SSSH.
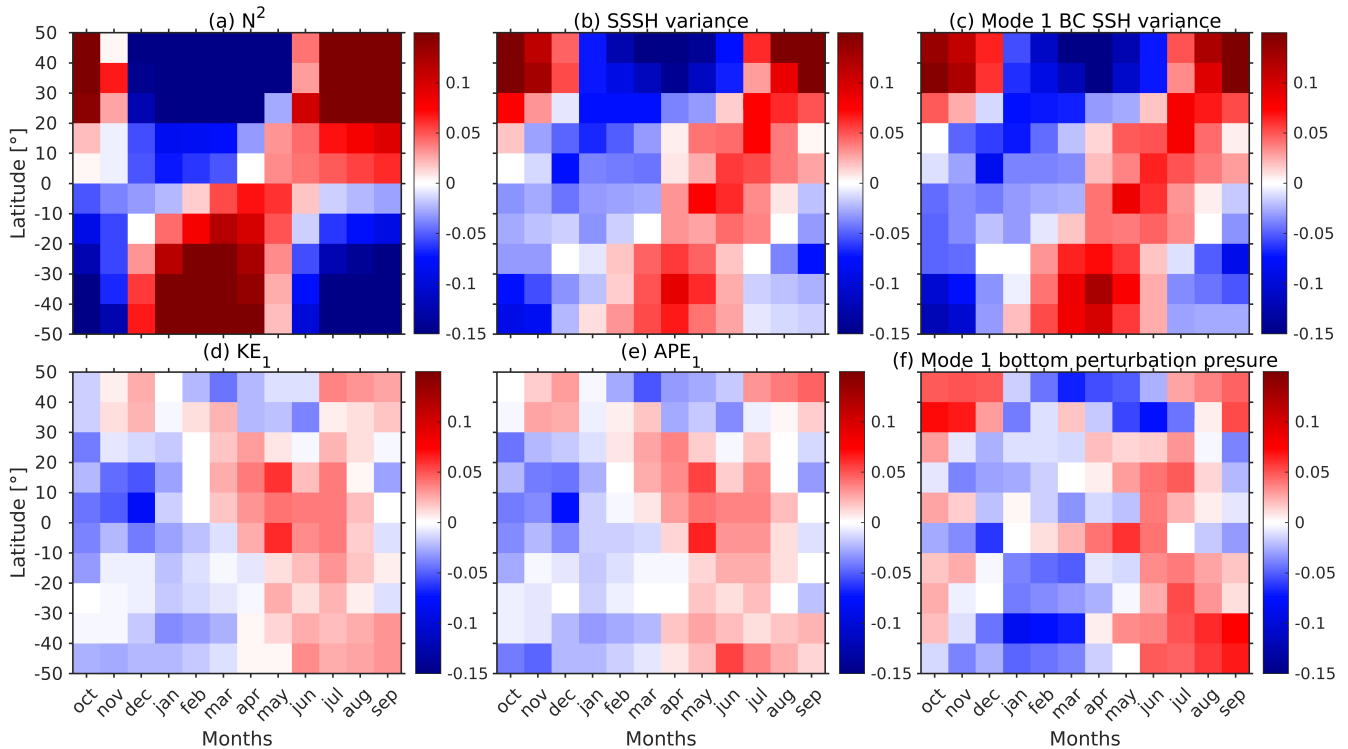
Figure 7. Zonally averaged normalized anomaly time series of monthly-mean (a) depth-mean N^2 and semidiurnal (b) undecomposed SSSH variance, (c) mode 1 SSH variance, (d) mode 1 KE, (e) mode 1 APE, and (f) mode 1 bottom perturbation pressure variance for the Pacific Ocean. The anomalies are computed by removing and normalizing by the annual-mean values. Data is from expt 06.1.

5 Conclusions

In this study, we compare the seasonal variability of semidiurnal steric sea surface height (SSSH) with internal tide energet-
375 ics, which are extracted from two non-data assimilative global Hybrid Coordinate Ocean Model (HYCOM) simulations. We analyze the seasonal trends in SSSH variance, barotropic to baroclinic conversion rate, kinetic energy (KE), available potential energy (APE), and pressure flux for semidiurnal internal tides. The seasonal variability in the HYCOM simulation is also compared with the satellite altimeter data of Zhao (2021).

The seasonal cycle of the semidiurnal SSSH variance is 180° out of phase in the Northern and Southern Hemispheres, which
380 indicates that stratification may be responsible for this seasonal variability. We find that the amplitude of the seasonal cycles is about 10-15% of the annual-mean values when zonally averaged. The strongest seasonal variability in the semidiurnal SSSH variance is observed in Georges Bank and the Arabian Sea.

We compare the seasonal trend in semidiurnal SSSH variance with depth-integrated semidiurnal barotropic to baroclinic energy conversion rate, baroclinic energy flux, KE, ~~APE, and energy~~and APE. The seasonal trends in the energy terms are
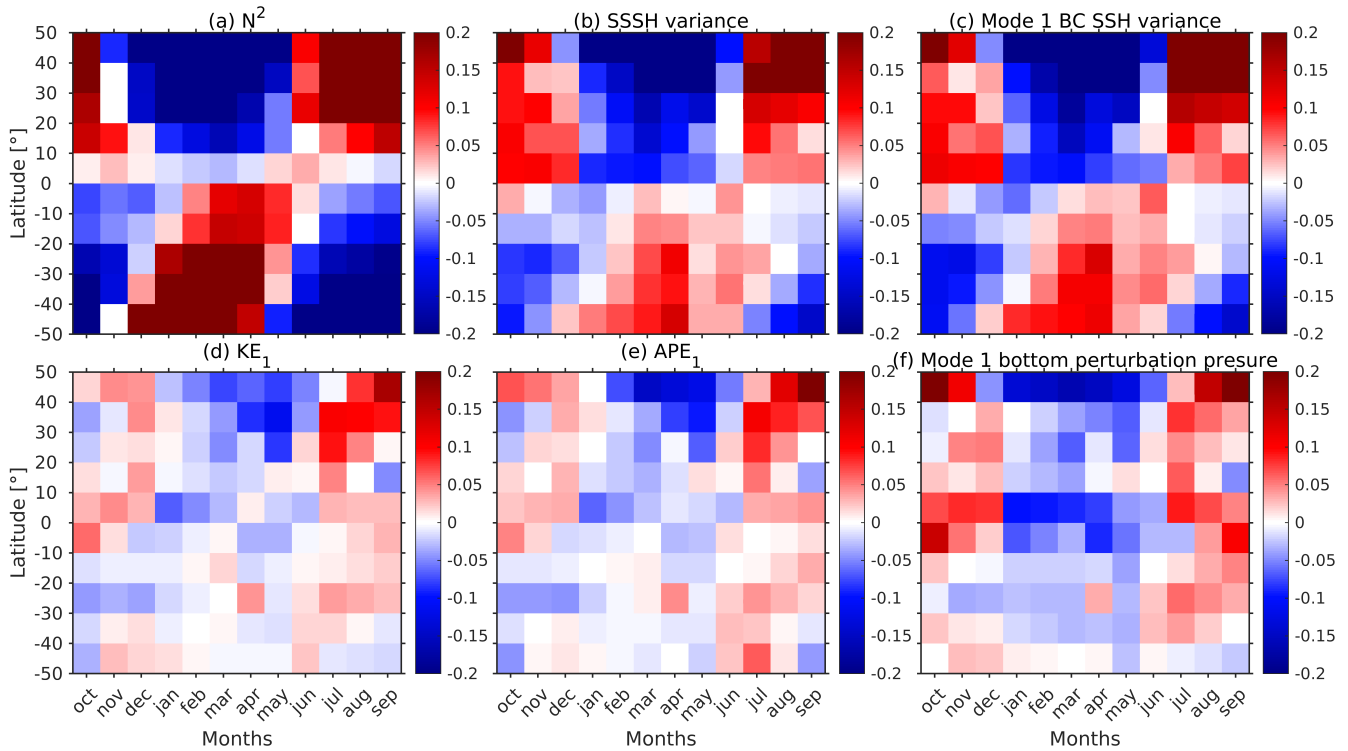
Figure 8. The same as Figure 7, but for the Atlantic Ocean.

385 quite similar. The conversion rate is dominant in influencing the seasonal variability ~~in~~ of the internal tide energetics. However, we observe differences in the seasonal cycles between SSSH variance and the energy terms. Seasonal maxima in energy terms and SSSH do not coincide in space and time. Moreover, the seasonal cycles in the Northern and Southern Hemispheres are not clearly out of phase as for SSSH. The seasonal ~~cycle~~ cycles of SSSH variance ~~, KE, and , conversion are only similar~~ and the energy terms are only in phase for Georges Bank and the Arabian Sea, where seasonal variability in internal tides is strong.

390 After comparing the seasonal variability in the HYCOM simulation with the satellite altimeter data from Zhao (2021), we find that the seasonal trends in M_2 internal tide SSH variance from the satellite altimeter data and the HYCOM simulation are quite similar. The trend observed in mode 1 M_2 KE from the HYCOM simulation is different from both the HYCOM and satellite altimeter mode 1 M_2 baroclinic SSH variance for both the Pacific and Atlantic Oceans. Therefore, we conclude that the seasonal variability in ~~KE~~ the energy terms is different from the internal tide SSH variability in most places.

395 Next, we investigate potential mechanisms that may explain the differences in the seasonal variability between semidiurnal SSSH variance and the energy terms. We explore the modulation of SSSH by the seasonal stratification. SSSH is strongly affected by the density of the surface layers, which varies significantly due to seasonal temperature changes. We compare the seasonal trends in semidiurnal SSSH variance with mode 1 semidiurnal SSH variance, bottom perturbation pressure variance, KE, APE, and buoyancy frequency. Although the seasonal cycles for both mode 1 SSH variance and the undecomposed SSSH
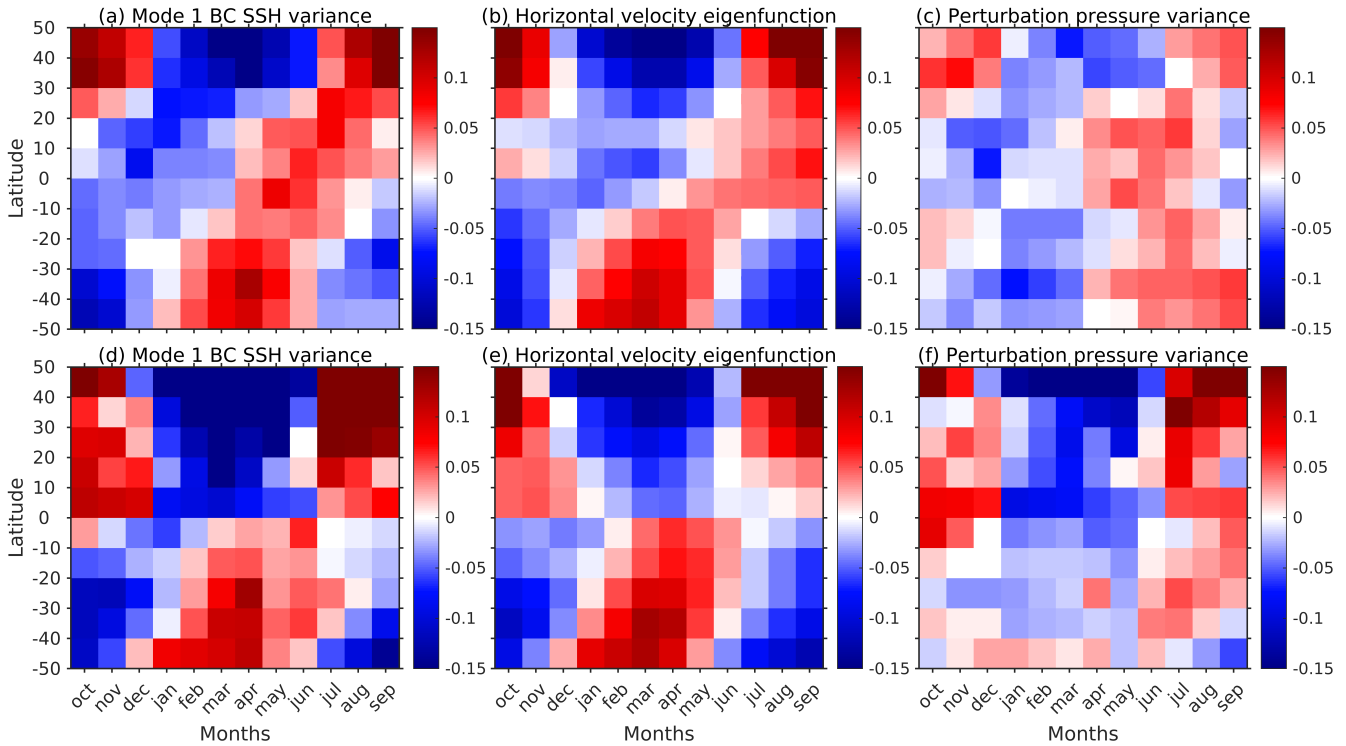
Figure 9. Zonally averaged normalized anomaly time series of (a and d) semidiurnal mode 1 baroclinic SSH variance, (b and e) mode 1 horizontal velocity eigenfunction ($\mathcal{U}_1^2$) at $z = 0$, and (c and f) semidiurnal mode 1 perturbation pressure amplitude ($\tilde{p_1}$) variance for the Pacific Ocean (top row) and Atlantic Ocean (bottom row). Data is from expt 06.1.

400   variance are similar, they differ from the mode 1 bottom perturbation pressure variance, KE, and APE. The seasonal cycle in the mode 1 SSH variance is mostly due to changes in the mode 1 horizontal velocity eigenfunction at the surface and not due to changes in the mode 1 perturbation pressure amplitude. The strong stratification in summer causes the horizontal velocity eigenfunction to be surface intensified, which leads to an increase in semidiurnal surface perturbation pressure and SSSH variance.

405   ~~According to our analysis, internal tide SSH, KE, and APE are different indicators of the seasonal variability of internal tides in the global ocean. They may represent various dynamic mechanisms of internal tide generation and propagation. However, we need to conduct further research to understand their relationships and seasonal patterns more accurately.~~

~~Our analysis also~~ Our analysis suggests that internal tide sea surface height may not be the most accurate indicator of the true seasonal variability of internal tides. Seasonal changes in the surface density stratification can modulate the seasonal variability

410   in sea surface height. Because surface density values and stratification also change on weekly to monthly time scales, it may be possible that the internal tide nonstationarity (Shriver et al., 2014; Zaron, 2017) is overestimated when considering sea surface

height. Nevertheless, sea surface height can still be useful in regions where there is a strong seasonal variability in internal tides, such as the Arabian Sea and Georges Bank.

Code and data availability. Some Hybrid Coordinate Ocean Model (HYCOM) simulation data and code is available at https://zenodo.org/records/1087103 (Kaur and Buijsman, 2024). The satellite altimeter dataset from Zhao (2021) is available at https://figshare.com/articles/dataset/Seasonal_ mode-1_M2_internal_tide_models/14759094.

Appendix A: Seasonal trends in semidiurnal steric sea surface height variance from expt 18.5

We compute the zonally averaged anomaly time series of steric sea surface height (SSSH) variance from expt 18.5 for all five years in a similar manner as for expt 06.1. We calculate the semidiurnal SSSH variance using the harmonic time series constructed for M_2, S_2, and N_2 for each one-month segment over areas with a seafloor depth greater than 100 m, average the variance over 10-degree latitude bins for the Atlantic and Pacific Oceans, and remove and average by the annual-mean variance. The seasonal variability observed in the five-year time series in Figure A1 closely resembles that of the one-year simulation expt 06.1 in Figures 3c and 4c. Similar to expt 06.1, the maximum SSSH variance occurs in the Northern Hemisphere in September and October, while the maximum variance in the Southern Hemisphere is observed in March and April. The only difference observed is in the Pacific Ocean at lower latitudes, which may be due to S_2 and K_2 aliasing. Note that the seasonal variability of the M_2 variance is the same for expt 18.5 and expt 06.1 (not shown). We also observe that the interannual variability is weak.

Appendix B: Seasonal trends in non-normalized energy terms and steric sea surface height variance

In this appendix, we show the seasonal trends ~~in~~ for the non-normalized semidiurnal barotropic to baroclinic conversion rate, baroclinic energy flux, ~~steric sea surface height (SSSH)~~ SSSH variance, baroclinic kinetic energy (KE), available potential energy (APE), and ~~energy~~ their sum for the Pacific and Atlantic Oceans in Figures B1 and B2, respectively. To compute the seasonal trends, we zonally average the conversion rate, flux, SSSH variance, KE, APE, and energy over 10-degree latitude bins for the Atlantic and the Pacific Oceans for each one-month segment. For all variables, shallow areas are removed (depth < 100 m). The anomalies are computed by removing the annual-mean values. The non-normalized anomalies look similar to the normalized plots in Figures 3 and 4, except at higher latitudes.

Appendix C: Georges Bank and the Arabian Sea

In Section 3.3, ~~it was observed~~ we show that KE, conversion rate, and SSSH variance exhibit similar seasonal trends in Georges Bank and the Arabian Sea (Figure 5i, j, o, and p). Furthermore, ~~it was found that~~ the seasonal variability is strongest in these two regions (Figure 2a and c). In this section, we ~~conduct a regional analysis of these regions~~ aim to understand the
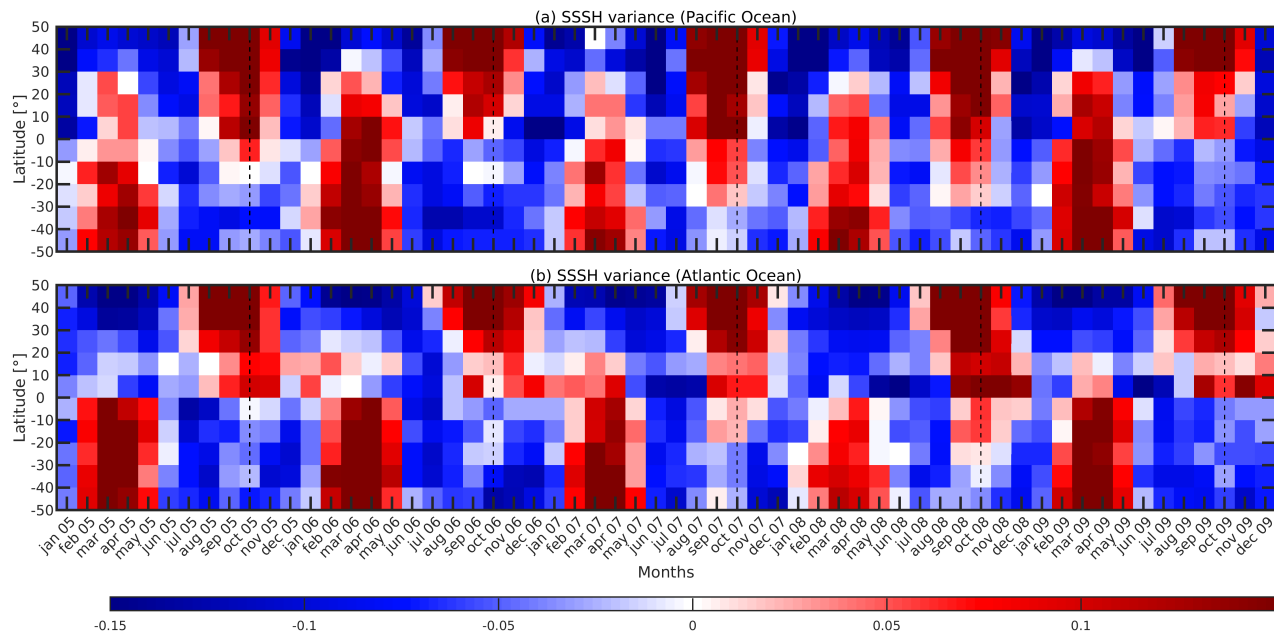
Figure A1. Zonally averaged anomaly time series of monthly variance of semidiurnal SSSH from expt 18.5 for the (a) Pacific and (b) Atlantic Oceans. The anomalies are computed by removing and normalizing by the annual-mean values.

mechanisms causing the seasonal variability in the semidiurnal internal tides in these areas. Specifically, we investigate the impact of changes in the vertical profile of stratification on the barotropic to baroclinic conversion throughout the year. To do this, we calculate the vertical profile of the conversion rate using the following equation (Kang and Fringer, 2012)

$$C_v(z) = \frac{1}{T} \int_0^T \rho'(z,t)gW(z,t)dt, \tag{C1}$$

where $W(z) = -W(z=-H)\frac{z}{H}$.

Georges Bank and the Gulf of Maine are located in the Northwest Atlantic Ocean. Internal tides are generated on the northeast flank of the Georges Bank and the Northeast Channel in this region ~~(Figure 1b; Chen et al., 2011; Schindelegger et al., 2022)~~ (Figure 1b) (Chen et al., 2011; Schindelegger et al., 2022). The M_2 barotropic tides are strong in this area, but there are only small seasonal changes in barotropic sea surface height amplitude (Godin, 1995; Katavouta et al., 2016). However, studies have reported seasonal changes in tides related to stratification in the Gulf of Maine (Chen et al., 2011; Katavouta et al., 2016; Shen et al., 2020; Schindelegger et al., 2022). To understand the mechanisms causing the seasonal variability, we compare the conversion rate and buoyancy frequency for the ~~point~~ location where the conversion rate is at its maximum (294.48°E; 42.09°N)~~where the conversion rate is at its maximum~~. We compare the ~~conversion rate calculated by two different methods described in~~ depth-integrated and monthly-mean conversion rates calculated with Eq. (6) (method 1) and Eq. (C1)
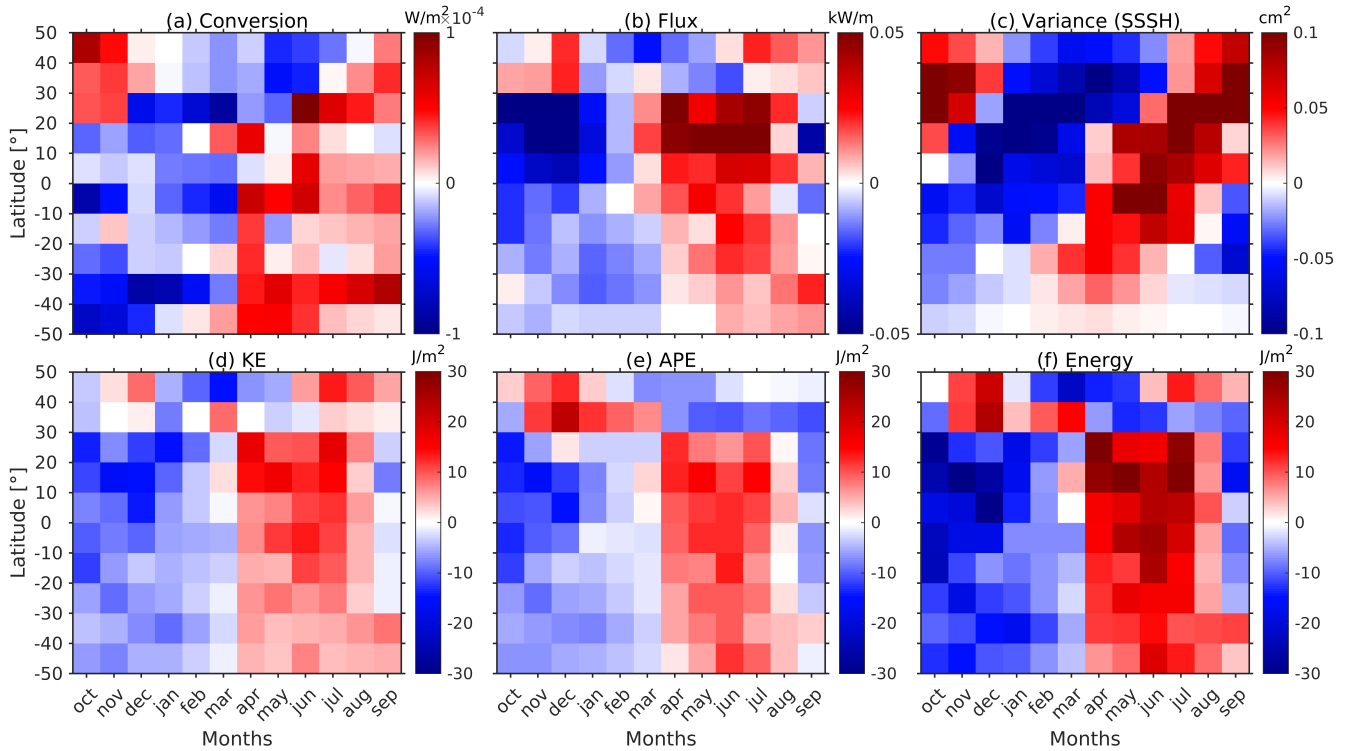
Figure B1. Zonally averaged anomaly time series of semidiurnal (a) barotropic to baroclinic conversion rate, (b) baroclinic energy flux, (c) SSSH variance, (d) KE, (e) APE, and (f) ~~energy~~ KE + APE for the Pacific Ocean. Data is from expt 06.1.

(method 2), and observe that both methods ~~give~~ yield similar values (Figure C1a). Additionally, we observe a similar seasonal cycle for the depth-integrated conversion rate and depth-averaged buoyancy frequency at this ~~point~~location. Interestingly, we discover that when stratification is ~~higher~~ stronger near the surface (depths less than 100 m), the conversion rate is also higher for those months throughout the entire water column (Figure C1c and e). ~~We believe this may be due to increased stratification in the surface layer during~~ The factors affecting stratification in Georges Bank are summer surface heating, surface heat transfer and cold winds during winter, interaction between the Gulf Stream and the ~~summer and fall when solar radiation in the region is at its highest~~southward movement of Labrador Sea water, and advection due to eddies (McLellan, 1957; Gatien, 1976; Brown and Beardsley, 1978; Csanady and Hamilton, 1988; Petrie and Drinkwater, 1993; Katavouta et al., .

In the Arabian Sea region, strong internal tides are generated on the shelf break, which generally propagate offshore ~~as beams~~ (Zhao, 2019; Zaron, 2019; Subeesh et al., 2021; Ma et al., 2021). On the slope, internal tides are stronger in March than in July due to the deepening of the pycnocline during the pre-monsoon period (Subeesh et al., 2021). In the Arabian Sea, the monsoonal winds, which change direction seasonally (Clemens et al., 1991), influence ocean circulation (Shetye et al., 1990, 1991; Beal et al., 2013) and are responsible for changes in pycnocline depth (Rudnick et al., 1997). We
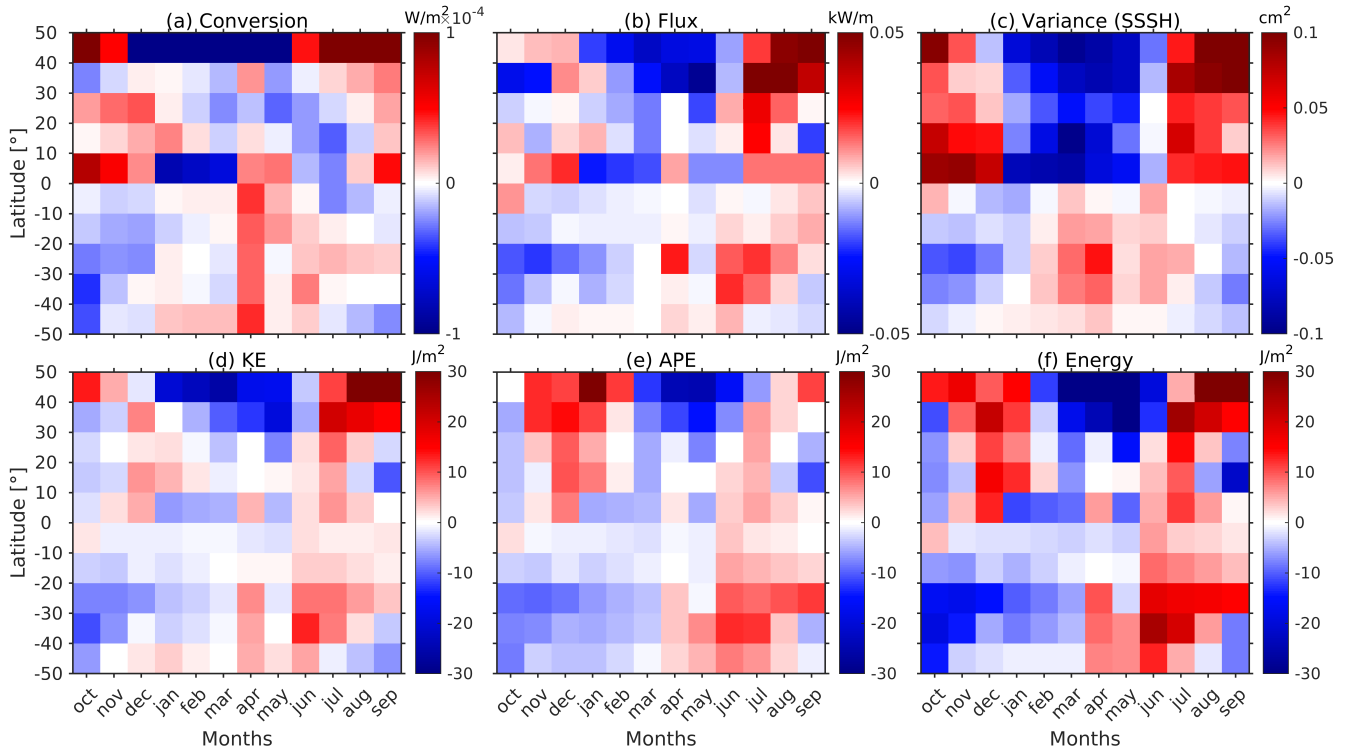
Figure B2. The same as Figure B1, but for the Atlantic Ocean.

compare the vertical profile of the barotropic to baroclinic conversion with buoyancy frequency in Figure C1 for a ~~site~~ location where the conversion rate is maximum (430.64°E; 18.24°N)~~, where the conversion rate is maximum~~. We get similar results for
470 the ~~conversion calculated using two methods mentioned in Eq. (6) and Eq. (C1)~~ depth-integrated and monthly-mean conversion rates calculated for the two methods as shown in Figure C1b. ~~The seasonal trend~~ In contrast to Georges Bank, the seasonal trends in depth-integrated conversion rate and depth-averaged buoyancy frequency are not similar. We observe that the conversion rate is large for the months where the magnitude of buoyancy frequency is high at the deeper depths (150-250 m) (Figure C1d and f).

475 ~~We conclude that seasonal variability in stratification at the generation site is impacting the barotropic to baroclinic conversion for both~~ In conclusion, at both Georges Bank and the Arabian Sea~~and Georges Bank. However, the surface stratification is responsible for seasonal changes in~~, the seasonality in stratification greatly affects the conversion. However, at Georges Bank, ~~while the vertical profile of buoyancy frequency is the primary factor for the Arabian Sea~~these stratification changes occur mainly at the surface, whereas in the Arabian Sea, these changes mostly take place at depth.
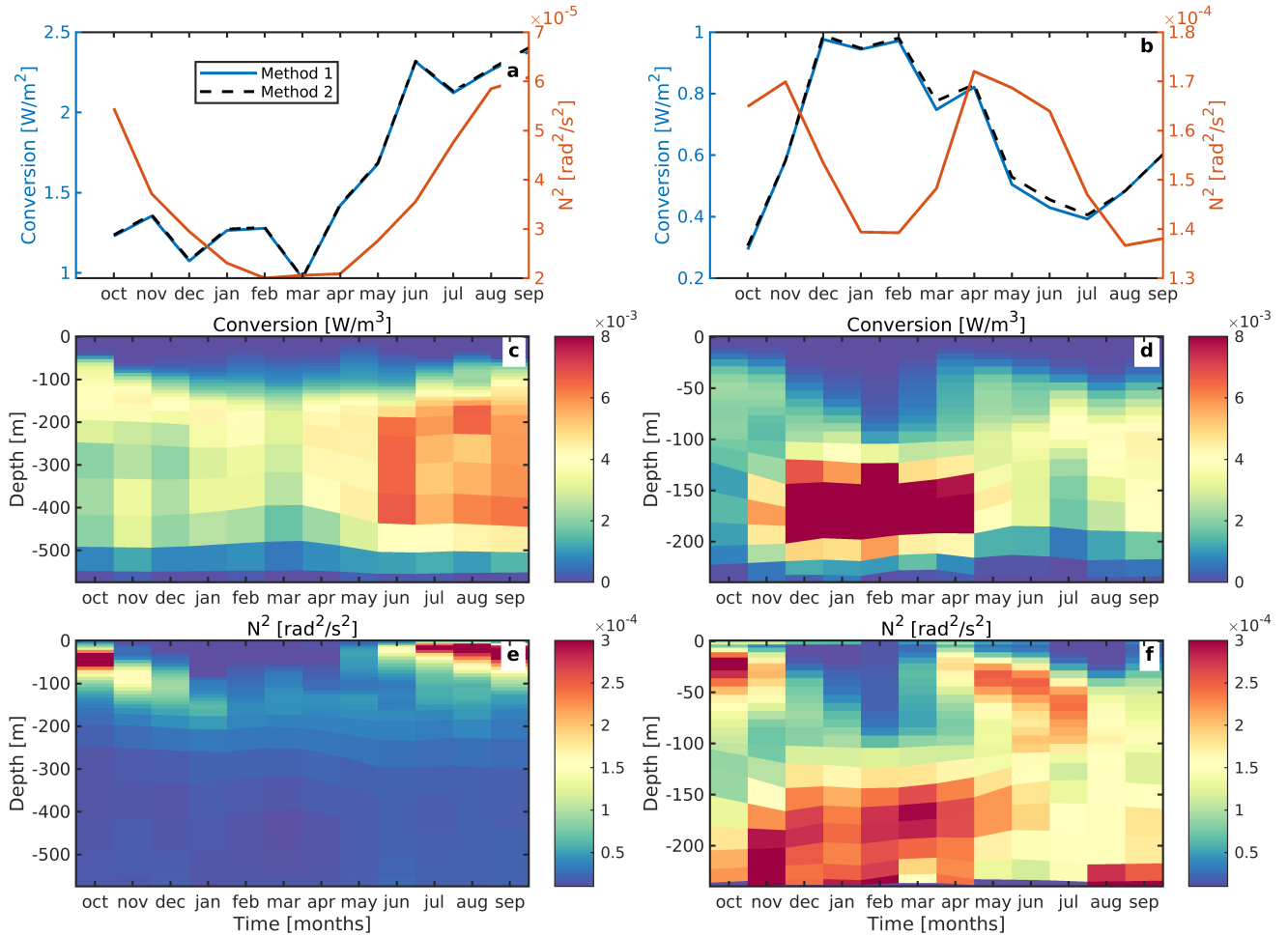
Figure C1. (a and b) Time series of monthly-mean depth-integrated conversion and depth-averaged buoyancy frequency for a ~~site~~ location on the shelf slope in Georges Bank (left column) and the Arabian Sea (right column). Methods 1 and 2 represent the depth-integrated conversion computed using Eq. (6) and Eq. (C1), respectively. (~~b~~c and d) Vertical conversion profile and (~~e~~e and f) vertical buoyancy frequency profile for ~~a site in~~ Georges Bank (left column) and the Arabian Sea (right column). Data is from expt 06.1.

480 *Author contributions.* HK processed the data, plotted the results, and wrote the first version of the manuscript. MB, ZZ, and JS collected and processed the data. All authors reviewed and edited the paper until its final version.

Competing interests. The authors declare that they have no conflict of interest.

Acknowledgements. Harpreet Kaur is funded by the National Aeronautics and Space Administration (NASA) grants 80NSSC18K0771 and 80NSSC20K1135, and Office of Naval Research (ONR) USA grant N00014-19-1-2704. Maarten Buijsman is funded by the National Aero-
485 nautics and Space Administration (NASA) grants 80NSSC18K0771 and 80NSSC20K1135, and Office of Naval Research (ONR) USA grants N00014-19-1-2704 and N00014-22-1-2576. Jay Shriver ~~was~~ is supported by Office of Naval Research (ONR) Grant N0001423WX01413, which is a component of the Global Internal Waves project of the National Oceanographic Partnership Program (https://nopp-giw.ucsd.edu/).

References

Alford, M. H. and Zhao, Z.: Global Patterns of Low-Mode Internal-Wave Propagation. Part I: Energy and Energy Flux, Journal of Physical Oceanography, 37, 1829 – 1848, https://doi.org/10.1175/JPO3085.1, 2007.

Ansong, J., Arbic, B. K., Buijsman, M., Richman, J., Shriver, J. F., and Wallcraft, A. J.: Indirect evidence for substantial damping of low-mode internal tides in the open ocean, Journal of Geophysical Research: Oceans, 120, https://doi.org/10.1002/2015JC010998, 2015.

Arbic, B. K., Wallcraft, A. J., and Metzger, E. J.: Concurrent simulation of the eddying general circulation and tides in a global ocean model, Ocean Modelling, 32, 175–187, https://doi.org/10.1016/j.ocemod.2010.01.007, 2010.

Baines, P.: On internal tide generation models, Deep Sea Research Part A. Oceanographic Research Papers, 29, 307–338, https://doi.org/10.1016/0198-0149(82)90098-X, 1982.

Beal, L. M., Hormann, V., Lumpkin, R., and Foltz, G. R.: The Response of the Surface Circulation of the Arabian Sea to Monsoonal Forcing, Journal of Physical Oceanography, 43, 2008 – 2022, https://doi.org/https://doi.org/10.1175/JPO-D-13-033.1, 2013.

Bij de Vaate, I., Vasulkar, A. N., Slobbe, D. C., and Verlaan, M.: The Influence of Arctic Landfast Ice on Seasonal Modulation of the M2 Tide, Journal of Geophysical Research: Oceans, 126, e2020JC016 630, https://doi.org/10.1029/2020JC016630, 2021.

Brown, W. S. and Beardsley, R. C.: Winter Circulation in the Western Gulf of Maine: Part 1. Cooling and Water Mass Formation, Journal of Physical Oceanography, 8, 265 – 277, https://doi.org/10.1175/1520-0485(1978)008<0265:WCITWG>2.0.CO;2, 1978.

Buijsman, M. C., Ansong, J., Arbic, B. K., Richman, J., Shriver, J., Timko, P., Wallcraft, A., Whalen, C., and Zhao, Z.: Impact of Parameterized Internal Wave Drag on the Semidiurnal Energy Balance in a Global Ocean Circulation Model, Journal of Physical Oceanography, 46, 1399–1419, https://doi.org/10.1175/JPO-D-15-0074.1, 2016.

Buijsman, M. C., Arbic, B. K., Richman, J. G., Shriver, J. F., Wallcraft, A. J., and Zamudio, L.: Semidiurnal internal tide incoherence in the equatorial Pacific, Journal of Geophysical Research: Oceans, 122, 5286–5305, https://doi.org/10.1002/2016JC012590, 2017.

Buijsman, M. C., Stephenson, G. R., Ansong, J. K., Arbic, B. K., Green, J. A. M., Richman, J. G., Shriver, J. F., Vic, C., Wallcraft, A. J., and Zhao, Z.: On the interplay between horizontal resolution and wave drag and their effect on tidal baroclinic mode waves in realistic global ocean simulations, Ocean Modelling, 152, 101656, https://doi.org/10.1016/j.ocemod.2020.101656, 2020.

Chen, C., Huang, H., Beardsley, R. C., Xu, Q., Limeburner, R., Cowles, G. W., Sun, Y., Qi, J., and Lin, H.: Tidal dynamics in the Gulf of Maine and New England Shelf: An application of FVCOM, Journal of Geophysical Research: Oceans, 116, https://doi.org/10.1029/2011JC007054, 2011.

Clemens, S., Prell, W., Murray, D., Shimmield, G., and Weedon, G.: Forcing mechanisms of the Indian Ocean monsoon, Nature, 353, 720–725, https://doi.org/10.1038/353720a0, 1991.

Colosi, J. and Munk, W.: Tales of the Venerable Honolulu Tide Gauge, Journal of Physical Oceanography, 36, https://doi.org/10.1175/JPO2876.1, 2006.

Csanady, G. and Hamilton, P.: Circulation of slopewater, Continental Shelf Research, 8, 565–624, https://doi.org/10.1016/0278-4343(88)90068-4, 1988.

de Lavergne, C., Falahat, S., Madec, G., Roquet, F., Nycander, J., and Vic, C.: Toward global maps of internal tide energy sinks, Ocean Modelling, 137, 52–75, https://doi.org/10.1016/j.ocemod.2019.03.010, 2019.

Duda, T. F., Lin, Y.-T., Buijsman, M., and Newhall, A. E.: Internal Tidal Modal Ray Refraction and Energy Ducting in Baroclinic Gulf Stream Currents, Journal of Physical Oceanography, 48, 1969 – 1993, https://doi.org/10.1175/JPO-D-18-0031.1, 2018.

Egbert, G. and Ray, R. D.: Semi-diurnal and diurnal tidal dissipation from TOPEX-POSEIDON altimetery, Geophysical Research Letters, 30, https://doi.org/10.1029/2003GL017676, 2003.

Gatien, M. G.: A Study in the Slope Water Region South of Halifax, Journal of the Fisheries Research Board of Canada, 33, 2213–2217, https://doi.org/10.1139/f76-270, 1976.

Gerkema, T. and Zimmerman, J. T. F.: An introduction to internal waves: Lecture Notes, R. Neth. Inst. for Sea Res., Den Burg., 2008.

Gerkema, T., Lam, F. P. A., and Maas, L. R. M.: Internal tides in the Bay of Biscay: conversion rates and seasonal effects, Deep Sea Research Part II: Topical Studies in Oceanography, 51, 2995 – 3008, https://doi.org/10.1016/j.dsr2.2004.09.012, 2004.

Godin, G.: Rapid evolution of the tide in the Bay of Fundy, Continental Shelf Research, 15, 369–372, https://doi.org/10.1016/0278-4343(93)E0005-S, 1995.

Hallberg, R.: A thermobaric instability of Lagrangian vertical coordinate ocean models, Ocean Modelling, 8, 279–300, https://doi.org/10.1016/j.ocemod.2004.01.001, 2005.

Hendershott, M. C.: The Effects of Solid Earth Deformation on Global Ocean Tides, Geophysical Journal International, 29, 389–402, https://doi.org/10.1111/j.1365-246X.1972.tb06167.x, 1972.

Hogan, T., Liu, M., Ridout, J., Peng, M., Whitcomb, T., Ruston, B., Reynolds, C., Eckermann, S., Moskaitis, J., Baker, N., McCormack, J., Viner, K., McLay, J., Flatau, M., Xu, L., Chen, C., and Chang, S.: The Navy Global Environmental Model, Oceanography, 27, 116–125, https://doi.org/10.5670/oceanog.2014.73, 2014.

Huess, V. and Andersen, O.: Seasonal variation in the main tidal constituent from Altimetry, Geophysical Research Letters, 28, 567–570, https://doi.org/10.1029/2000GL011921, 2001.

Huthnance, J. M.: Waves and currents near the continental shelf edge, Progress In Oceanography, 10, 193–226, https://doi.org/10.1016/0079-6611(81)90004-5, 1981.

Jan, S., Lien, R.-C., and Ting, C.-H.: Numerical Study of Baroclinic Tides in Luzon Strait, Journal of Oceanography, 64, 789–802, https://doi.org/10.1007/s10872-008-0066-5, 2008.

Jayne, S. R. and St. Laurent, L. C.: Parameterizing tidal dissipation over rough topography, Geophysical Research Letters, 28, 811–814, https://doi.org/10.1029/2000GL012044, 2001.

Kang, D. and Fringer, O.: Energetics of Barotropic and Baroclinic Tides in the Monterey Bay Area, Journal of Physical Oceanography, 42, 272–290, https://doi.org/10.1175/JPO-D-11-039.1, 2012.

Kang, S. K., Foreman, M. G. G., Lie, H.-J., Lee, J.-H., Cherniawsky, J., and Yum, K.-D.: Two-layer tidal modeling of the Yellow and East China Seas with application to seasonal variability of the M2 tide, Journal of Geophysical Research: Oceans, 107, https://doi.org/10.1029/2001JC000838, 2002.

Katavouta, A., Thompson, K. R., Lu, Y., and Loder, J. W.: Interaction between the Tidal and Seasonal Variability of the Gulf of Maine and Scotian Shelf Region, Journal of Physical Oceanography, 46, 3279 – 3298, https://doi.org/10.1175/JPO-D-15-0091.1, 2016.

Kaur, H.: Variability in Semidiurnal Surface and Internal Tides in Global Ocean Model Simulations, Dissertations, 2242, https://aquila.usm.edu/dissertations/2242, 2024.

Kaur, H. and Buijsman, M.: The Seasonal Variability in the Semidiurnal Internal Tide; A Comparison between Sea Surface Height and Energetics [Data set], Zenodo, https://doi.org/10.5281/zenodo.10871038, 2024.

Kelly, S. M., Nash, J. D., Martini, K. I., Alford, M. H., and Kunze, E.: The Cascade of Tidal Energy from Low to High Modes on a Continental Slope, Journal of Physical Oceanography, 42, 1217 – 1232, https://doi.org/10.1175/JPO-D-11-0231.1, 2012.

Liu, J., He, Y., Wang, D., Liu, T., and Cai, S.: Observed enhanced internal tides in winter near the Luzon Strait, Journal of Geophysical Research: Oceans, 120, 6637–6652, https://doi.org/10.1002/2015JC011131, 2015.

Löb, J., Köhler, J., Mertens, C., Walter, M., Li, Z., Storch, J.-S., Zhao, Z., and Rhein, M.: Observations of the Low-Mode Internal Tide and Its Interaction With Mesoscale Flow South of the Azores, Journal of Geophysical Research: Oceans, 125, https://doi.org/10.1029/2019JC015879, 2020.

Ma, J., Guo, D., Zhan, P., and Hoteit, I.: Seasonal M2 Internal Tides in the Arabian Sea, Remote Sensing, 13, 2823, https://doi.org/10.3390/rs13142823, 2021.

McLellan, H. J.: On the Distinctness and Origin of the Slope Water off the Scotian Shelf and its Easterly Flow South of the Grand Banks, Journal of the Fisheries Research Board of Canada, 14, 213–239, https://doi.org/10.1139/f57-011, 1957.

Melet, A., Legg, S., and Hallberg, R.: Climatic Impacts of Parameterized Local and Remote Tidal Mixing, Journal of Climate, 29, 3473 – 3500, https://doi.org/10.1175/JCLI-D-15-0153.1, 2016.

Metzger, E., Hurlburt, H., Xu, X., Shriver, J. F., Gordon, A., Sprintall, J., Susanto, R., and van Aken, H.: Simulated and observed circulation in the Indonesian Seas: 1/12° global HYCOM and the INSTANT observations, Dynamics of Atmospheres and Oceans, 50, 275–300, https://doi.org/10.1016/j.dynatmoce.2010.04.002, 2010.

Mukherjee, S., Wilson, D., Jobsis, P., and Habtes, S.: Numerical modeling of internal tides and submesoscale turbulence in the US Caribbean regional ocean, Scientific Reports, 13, 1091, https://doi.org/10.1038/s41598-023-27944-2, 2023.

Munk, W. and Wunsch, C.: Abyssal recipes II: energetics of tidal and wind mixing, Deep Sea Research Part I: Oceanographic Research Papers, 45, 1977 – 2010, https://doi.org/10.1016/S0967-0637(98)00070-3, 1998.

Müller, M., Cherniawsky, J., Foreman, M., and Storch, J.-S.: Global M2 internal tide and its seasonal variability from high resolution ocean circulation and tide modeling, Geophysical Research Letters, 39, https://doi.org/10.1029/2012GL053320, 2012.

Nash, J. D., Alford, M. H., and Kunze, E.: Estimating Internal Wave Energy Fluxes in the Ocean, Journal of Atmospheric and Oceanic Technology, 22, 1551 – 1570, https://doi.org/10.1175/JTECH1784.1, 2005.

Nelson, A., Arbic, B. K., Zaron, E., Savage, A., Richman, J., Buijsman, M., and Shriver, J.: Toward Realistic Nonstationarity of Semidiurnal Baroclinic Tides in a Hydrodynamic Model, Journal of Geophysical Research: Oceans, 124, https://doi.org/10.1029/2018JC014737, 2019.

Ngodock, H. E., Souopgui, I., Wallcraft, A. J., Richman, J. G., Shriver, J. F., and Arbic, B. K.: On improving the accuracy of the M2 barotropic tides embedded in a high-resolution global ocean circulation model, Ocean Modelling, 97, 16 – 26, https://doi.org/10.1016/j.ocemod.2015.10.011, 2016.

Osborne, J. J., Kurapov, A. L., Egbert, G. D., and Kosro, P. M.: Spatial and Temporal Variability of the M2 Internal Tide Generation and Propagation on the Oregon Shelf, Journal of Physical Oceanography, 41, 2037 – 2062, https://doi.org/10.1175/JPO-D-11-02.1, 2011.

Petrie, B. and Drinkwater, K.: Temperature and salinity variability on the Scotian Shelf and in the Gulf of Maine 1945–1990, Journal of Geophysical Research: Oceans, 98, 20 079–20 089, https://doi.org/10.1029/93JC02191, 1993.

Ponte, A. L. and Klein, P.: Incoherent signature of internal tides on sea level in idealized numerical simulations, Geophysical Research Letters, 42, 1520–1526, https://doi.org/10.1002/2014GL062583, 2015.

Qu, T. and Melnichenko, O.: Steric Changes Associated With the Fast Sea Level Rise in the Upper South Indian Ocean, Geophysical Research Letters, 50, e2022GL100 635, https://doi.org/10.1029/2022GL100635, 2023.

Rainville, L. and Pinkel, R.: Propagation of Low-Mode Internal Waves through the Ocean, Journal of Physical Oceanography, 36, 1220–1236, https://doi.org/10.1175/JPO2889.1, 2006.

Raja, K. J., Buijsman, M. C., Shriver, J. F., Arbic, B. K., and Siyanbola, O.: Near-Inertial Wave Energetics Modulated by Background Flows in a Global Model Simulation, Journal of Physical Oceanography, 52, 823 – 840, https://doi.org/10.1175/JPO-D-21-0130.1, 2022.

600 Ray, R. D.: Ocean self-attraction and loading in numerical tidal models, Marine Geodesy, 21, 181–192, https://doi.org/10.1080/01490419809388134, 1998.

Ray, R. D. and Zaron, E.: Non-Stationary Internal Tides Observed Using Dual-Satellite Altimetry, Geophysical Research Letters, 38, https://doi.org/10.1029/2011GL048617, 2011.

Rosmond, T., Teixeira, J., Peng, M., Hogan, T., and Pauley, R.: Navy Operational Global Atmospheric Prediction System (NOGAPS):
605 Forcing for Ocean Models, Oceanography, 15, 99–108, https://doi.org/10.5670/oceanog.2002.40, 2002.

Rudnick, D. L., Weller, R. A., Eriksen, C. C., Dickey, T. D., Marra, J., and Langdon, C.: Moored instruments weather Arabian Sea monsoons, yield data, Eos, Transactions American Geophysical Union, 78, 117–121, https://doi.org/10.1029/97EO00073, 1997.

Savage, A., Arbic, B. K., Richman, J., Shriver, J., Alford, M., Buijsman, M., Farrar, J., Sharma, H., Voet, G., Wallcraft, A., and Zamudio,
L.: Frequency content of sea surface height variability from internal gravity waves to mesoscale eddies, Journal of Geophysical Research:
610 Oceans, https://doi.org/10.1002/2016JC012331, 2017.

Schindelegger, M., Kotzian, D. P., Ray, R. D., Green, J. A. M., and Stolzenberger, S.: Interannual Changes in Tidal Conversion Modulate M2 Amplitudes in the Gulf of Maine, Geophysical Research Letters, 49, e2022GL101 671, https://doi.org/10.1029/2022GL101671, 2022.

Shen, H., Perrie, W., and Johnson, C. L.: Predicting Internal Solitary Waves in the Gulf of Maine, Journal of Geophysical Research: Oceans, 125, e2019JC015 941, https://doi.org/10.1029/2019JC015941, 2020.

615 Shetye, S., Gouveia, A., Shenoi, S., Sundar, D., Michael, G. S., Almeida, A., and Santanam, K.: Hydrography and circulation off the west coast of India during the Southwest Monsoon 1987, Journal of Marine Research, 48, https://doi.org/10.1357/002224090784988809, 1990.

Shetye, S., Gouveia, A., Shenoi, S., Michael, G., Sundar, D., Almeida, A., and Santanam, K.: The coastal current off western India during the northeast monsoon, Deep Sea Research Part A. Oceanographic Research Papers, 38, 1517–1529, https://doi.org/10.1016/0198-0149(91)90087-V, 1991.

620 Shriver, J., Arbic, B. K., Richman, J., Ray, R., Metzger, E., Wallcraft, A., and Timko, P.: An evaluation of the barotropic and internal tides in a high-resolution global ocean circulation model, Journal of Geophysical Research, 117, C10 024, https://doi.org/10.1029/2012JC008170, 2012.

Shriver, J., Richman, J., and Arbic, B. K.: How stationary are the internal tides in a high-resolution global ocean circulation model?, Journal of Geophysical Research: Oceans, 119, https://doi.org/10.1002/2013JC009423, 2014.

625 Sinnett, G., Feddersen, F., Lucas, A. J., Pawlak, G., and Terrill, E.: Observations of Nonlinear Internal Wave Run-Up to the Surfzone, Journal of Physical Oceanography, 48, 531 – 554, https://doi.org/10.1175/JPO-D-17-0210.1, 2018.

Siyanbola, O. Q., Buijsman, M. C., Delpech, A., Renault, L., Barkan, R., Shriver, J. F., Arbic, B. K., and McWilliams, J. C.: Remote internal wave forcing of regional ocean simulations near the U.S. West Coast, Ocean Modelling, 181, 102 154, https://doi.org/10.1016/j.ocemod.2022.102154, 2023.

630 Siyanbola, O. Q., Buijsman, M. C., Delpech, A., Barkan, R., Pan, Y., and Arbic, B. K.: Interactions of Remotely Generated Internal Tides With the U.S. West Coast Continental Margin, Journal of Geophysical Research: Oceans, 129, e2023JC020 859, https://doi.org/10.1029/2023JC020859, 2024.

Solano, M. S., Buijsman, M. C., Shriver, J. F., Magalhaes, J., da Silva, J., Jackson, C., Arbic, B. K., and Barkan, R.: Nonlinear Internal Tides in a Realistically Forced Global Ocean Simulation, Journal of Geophysical Research: Oceans, 128, e2023JC019 913,
635 https://doi.org/10.1029/2023JC019913, 2023.

St. Laurent, L. and Garrett, C.: The Role of Internal Tides in Mixing the Deep Ocean, J. Phys. Oceanogr., 32, 2882–2899, https://doi.org/10.1175/1520-0485(2002)032<2882:TROITI>2.0.CO;2, 2002.

St. Laurent, P., Saucier, F. J., and Dumais, J.-F.: On the modification of tides in a seasonally ice-covered sea, Journal of Geophysical Research: Oceans, 113, https://doi.org/10.1029/2007JC004614, 2008.

640 Subeesh, M., Unnikrishnan, A., and Francis, P.: Generation, propagation and dissipation of internal tides on the continental shelf and slope off the west coast of India, Continental Shelf Research, 214, 104 321, https://doi.org/10.1016/j.csr.2020.104321, 2021.

Tuerena, R. E., Williams, R. G., Mahaffey, C., Vic, C., Green, J. A. M., Naveira-Garabato, A., Forryan, A., and Sharples, J.: Internal Tides Drive Nutrient Fluxes Into the Deep Chlorophyll Maximum Over Mid-ocean Ridges, Global Biogeochemical Cycles, 33, 995–1009, https://doi.org/10.1029/2019GB006214, 2019.

645 Waterhouse, A. F., MacKinnon, J. A., Nash, J. D., Alford, M. H., Kunze, E., Simmons, H. L., Polzin, K. L., Laurent, L. C. S., Sun, O. M., Pinkel, R., Talley, L. D., Whalen, C. B., Huussen, T. N., Carter, G. S., Fer, I., Waterman, S., Garabato, A. C. N., Sanford, T. B., and Lee, C. M.: Global Patterns of Diapycnal Mixing from Measurements of the Turbulent Dissipation Rate, Journal of Physical Oceanography, 44, 1854 – 1872, https://doi.org/10.1175/JPO-D-13-0104.1, 2014.

Yadidya, B., Arbic, B. K., Shriver, J. F., Nelson, A. D., Zaron, E. D., Buijsman, M. C., and Thakur, R.: Phase-Accurate Internal Tides
650 in a Global Ocean Forecast Model: Potential Applications for Nadir and Wide-Swath Altimetry, Geophysical Research Letters, 51, e2023GL107 232, https://doi.org/10.1029/2023GL107232, 2024.

Yan, T., Qi, Y., Jing, Z., and Cai, S.: Seasonal and Spatial Features of Barotropic and Baroclinic Tides in the Northwestern South China Sea, Journal of Geophysical Research (Oceans), 125, e14860, https://doi.org/10.1029/2018JC014860, 2020.

Zaron, E. D.: Mapping the Nonstationary Internal Tide with Satellite Altimetry, Journal of Geophysical Research, 122, 539–554,
655 https://doi.org/10.1002/2016JC012487, 2017.

Zaron, E. D.: Baroclinic Tidal Sea Level from Exact-Repeat Mission Altimetry, Journal of Physical Oceanography, 49, 193 – 210, https://doi.org/10.1175/JPO-D-18-0127.1, 2019.

Zaron, E. D. and Egbert, G. D.: Time-Variable Refraction of the Internal Tide at the Hawaiian Ridge, Journal of Physical Oceanography, 44, 538–557, https://doi.org/10.1175/JPO-D-12-0238.1, 2014.

660 Zaron, E. D. and Ray, R. D.: Clarifying the Distinction between Steric and Baroclinic Sea Surface Height, Journal of Physical Oceanography, 53, 2591 – 2596, https://doi.org/10.1175/JPO-D-23-0073.1, 2023.

Zhao, Z.: Mapping Internal Tides From Satellite Altimetry Without Blind Directions, Journal of Geophysical Research, 124, 8605–8625, https://doi.org/10.1029/2019JC015507, 2019.

Zhao, Z.: Seasonal mode-1 M2 internal tides from satellite altimetry, Journal of Physical Oceanography, https://doi.org/10.1175/JPO-D-21-
665 0001.1, 2021.

Zhao, Z. and Qiu, B.: Seasonal West-East Seesaw of M2 Internal Tides From the Luzon Strait, Journal of Geophysical Research: Oceans, 128, https://doi.org/10.1029/2022JC019281, 2023.

Zhao, Z., Wang, J., Menemenlis, D., Fu, L.-L., Chen, S., and Qiu, B.: Decomposition of the Multimodal Multidirectional M2 Internal Tide Field, Journal of Atmospheric and Oceanic Technology, 36, 1157 – 1173, https://doi.org/10.1175/JTECH-D-19-0022.1, 2019.